Research Square

Preprints are preliminary reports that have not undergone peer review.
They should not be considered conclusive, used to inform clinical practice,
or referenced by the media as validated information.

Optimization of SiO2 Nanoparticle concentration in Woven CFRP/Epoxy Composites for Hydrokinetic Turbine Blade Applications

Ravinthiran A

ravinthiran.mech@sairam.edu.in

Sri Sai Ram Engineering College

Vijaya Ramnath B

Sri Sai Ram Engineering College

Research Article

Keywords: CFRP/epoxy, SiO2 nanoparticles, mechanical properties, interlaminar shear strength, DMA, DSC, TGA, fatigue, SEM, EDS, hydrokinetic turbine blade

Posted Date: November 9th, 2026

DOI: https://doi.org/10.21203/rs.3.rs-11083003/v1

License: This work is licensed under a Creative Commons Attribution 4.0 International License.
Read Full License

Additional Declarations: No competing interests reported.

Optimization of SiO_2 Nanoparticle concentration in Woven CFRP/Epoxy Composites for Hydrokinetic Turbine Blade Applications

Ravinthiran A[1], Vijaya Ramnath B[2]

[1,2]Department of Mechanical Engineering, Sri Sai Ram Engineering College, Chennai, Tamil Nadu, India

[1]Research Scholar, Faculty of Mechanical Engineering, Anna University, Chennai, Tamil Nadu, India

Corresponding author: Ravinthiran A

Corresponding author email: ravinthiran.mech@sairam.edu.in

Corresponding author ORCID ID: https://orcid.org/0000-0001-7994-1409

Abstract

Carbon fibre reinforced epoxy (CFRP/epoxy) laminates are promising candidates for hydrokinetic turbine blades owing to their high specific stiffness, strength, corrosion resistance, and design flexibility. This study systematically investigates the concentration-dependent influence of SiO_2 nanoparticles incorporated into the epoxy phase of a ten-ply plain-woven CFRP laminate at concentrations of 0–4 wt%. Six formulations (C0, C0.5, C1, C2, C3, and C4) were fabricated using ultrasonic nanoparticle dispersion followed by vacuum-assisted resin infusion. Physical characteristics, microstructural features, elemental composition, chemical structure, mechanical properties, thermo-mechanical behaviour, fatigue resistance, and representative blade-level structural response were evaluated. Tensile, flexural, and interlaminar shear properties were determined according to ASTM D3039/D3039M, ASTM D790, and ASTM D2344/D2344M, respectively, while SEM/EDS, FTIR, XRD, DMA, DSC, TGA, and coefficient of thermal expansion measurements were employed for comprehensive characterization. The optimum performance was obtained at 2 wt% SiO_2 (C2), with tensile strength, flexural strength, and interlaminar shear strength increasing from 612 to 674 MPa, 748 to 835 MPa, and 46.2 to 54.3 MPa, respectively. The DMA glass-transition temperature increased from 108.4 to 116.8 °C, while storage modulus at 80 °C increased from 34.5 to 42.8

GPa. The 5% mass-loss temperature increased from 342 to 353 °C, and fatigue life at 0.65 UTS increased from 74,000 to 142,000 cycles. Higher nanoparticle concentrations diminished these improvements, attributed to particle clustering and matrix heterogeneity. Blade-level analysis further indicated reduced root-region stress and tip deflection for C2. Overall, 2 wt% SiO_2 provides a favourable material formulation for lightweight hydrokinetic turbine blade applications.

Keywords: CFRP/epoxy; SiO_2 nanoparticles; mechanical properties; interlaminar shear strength; DMA; DSC; TGA; fatigue; SEM; EDS; hydrokinetic turbine blade.

1. Introduction

Hydrokinetic turbines extract useful energy directly from moving water and therefore operate under a combination of hydrodynamic loading, cyclic bending, vibration and repeated changes in local flow conditions. Unlike many terrestrial structures, the turbine blade is simultaneously a fluid dynamic surface and a load bearing composite structure. Material stiffness affects the ability of the blade to preserve its intended hydrofoil geometry, while strength, interlaminar resistance and fatigue behaviour govern structural reliability. Recent assessments of hydrokinetic blade materials emphasize the need to balance specific mechanical performance, environmental resistance, manufacturability and life-cycle considerations [1,2].

Fibre reinforced polymer composites are attractive in this setting because the reinforcement architecture can be tailored to carry loads along preferred directions without the mass penalty associated with many metallic blade materials. Carbon fibres provide high tensile stiffness and strength at relatively low density, while epoxy provides fibre wetting, load transfer and matrix protection. However, the anisotropy of laminated CFRP means that a high fibre-direction tensile strength does not by itself guarantee resistance to matrix cracking, interlaminar shear failure or fatigue damage. For turbine blades, these matrix- and interface-dominated responses can become decisive when cyclic bending and local stress concentrations occur near roots, thickness transitions and bonded regions [1–4].

The epoxy matrix is therefore an important target for material modification. The matrix controls load transfer between adjacent carbon-fibre bundles, contributes to interlaminar shear strength

and governs a large part of the viscoelastic response. Matrix stiffness decreases as temperature approaches the glass transition region, and the resulting reduction in structural rigidity can influence blade deformation. Consequently, a useful modification strategy should improve both room temperature mechanical properties and the thermo mechanical stability of the cured polymer network.

Nanoscale inorganic fillers have emerged as a practical route for modifying epoxy matrices. SiO_2 is particularly attractive because it is thermally stable, chemically relatively inert and capable of interacting with the surrounding polymer network through its high specific surface area. Published nanosilica/epoxy studies generally report a non-monotonic concentration effect: low-to-moderate additions can increase stiffness, strength and fracture resistance, whereas excessive loading can promote particle agglomeration, viscosity growth, incomplete wetting and local stress concentration [5–10]. The optimum concentration is therefore not universal and must be established for a particular resin, fibre architecture and processing route. (Fig. 13)

The underlying reinforcement mechanisms are commonly associated with restriction of polymer-chain mobility, increased interphase constraint, crack deflection and crack branching. At sufficiently low concentrations, well-dispersed nanoparticles provide a large interfacial area through which stress can be redistributed. At higher concentrations, however, the same high surface area can become detrimental if particles cluster. Such clusters create heterogeneous regions and may behave as preferential sites for crack initiation. These competing mechanisms explain the rise-and-fall response often observed in tensile, flexural and interlaminar properties [7–11].

Although nanosilica modification has been widely investigated in neat epoxy and in selected fibre-reinforced systems, fewer studies connect the concentration-dependent material response to a hydrokinetic blade context using a coordinated mechanical and thermo-mechanical programme. In particular, the combination of tensile strength, flexural strength, ILSS, DMA, DSC, TGA, thermal expansion, fatigue and fracture morphology provides a more complete basis for selecting a blade material than any single property alone. This is especially important because the formulation that maximizes tensile strength may not necessarily maximize interlaminar resistance or thermal stability.

The present work therefore focuses specifically on the dry-state mechanical and thermo-mechanical response of woven CFRP/epoxy laminates modified with 0–4 wt% SiO_2

nanoparticles. The study deliberately separates these questions from hydrothermal durability, which is addressed in a companion paper. The central hypothesis is that an intermediate SiO_2 concentration will produce the best balance between dispersion and matrix/interphase reinforcement, while higher concentrations will progressively lose effectiveness because of clustering and processing-induced heterogeneity. The objectives are, Fabricate woven CFRP/epoxy laminates containing 0, 0.5, 1, 2, 3 and 4 wt% SiO_2 under controlled processing conditions, Quantify density, fibre volume fraction and void content to establish laminate quality, Correlate SEM/EDS, FTIR and XRD observations with concentration dependent mechanical behavior, Determine tensile, flexural and interlaminar shear properties and identify the optimum formulation, Evaluate Tg, storage modulus, damping, DSC transition, TGA degradation characteristics and thermal expansion, Assess tension–tension fatigue response of the reference and optimum formulations, Demonstrate the structural relevance of the optimized material through a representative hydrokinetic blade finite-element assessment.

The principal contribution is the identification of a single formulation 2 wt% SiO_2 that consistently maximizes the combined mechanical and thermo-mechanical response within the investigated composition range. Rather than treating nanoparticle reinforcement as a monotonic filler effect, the study links laminate quality, fracture morphology, interlaminar performance, viscoelastic response and cyclic damage resistance to the same concentration-dependent mechanism. This integrated approach provides a defensible materials-selection framework for hydrokinetic blade structures and establishes the dry-state baseline required for the companion hydrothermal-durability investigation. (Figure 1)

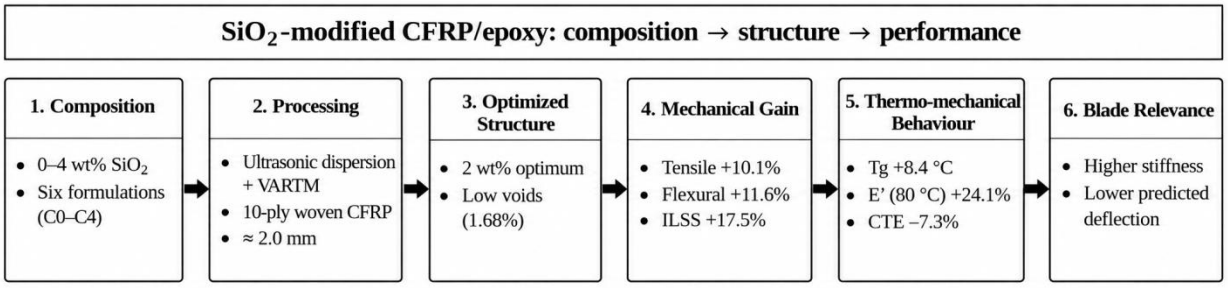


Figure 1. Graphical representation of the study design and principal outcomes.

2. Materials and Experimental Methods

2.1 Constituent materials

A plain woven carbon fibre fabric was used as the primary reinforcement. The area density was 200 g/m², with an average fibre diameter of approximately 7 μm and a fibre density of approximately 1.78 g/cm³. The balanced woven architecture provided approximately equal warp and weft reinforcement and was maintained for every formulation.

A DGEBA based epoxy resin was used as the matrix with an amine based curing agent. The resin density was approximately 1.10–1.15 g/cm³ and the viscosity approximately 800–1200 mPa·s at 25 °C. Resin and hardener were mixed at a 100:30 weight ratio. Commercial SiO_2 nanoparticles with an average particle size of approximately 30 nm, purity above 99% and density of approximately 2.20 g/cm³ were used as the secondary reinforcement. Table 1 shows Formulation and specifications of CFRP–SiO2 composite laminates.

Table 1. Formulation and specifications of CFRP–SiO_2 composite laminates.

Formulation	SiO2 (wt%)	Fibre architecture	Thickness
C0	0	10-ply plain woven, 0°/90°	2.0 ± 0.1 mm
C0.5	0.5	10-ply plain woven, 0°/90°	2.0 ± 0.1 mm
C1	1	10-ply plain woven, 0°/90°	2.0 ± 0.1 mm
C2	2	10-ply plain woven, 0°/90°	2.0 ± 0.1 mm
C3	3	10-ply plain woven, 0°/90°	2.0 ± 0.1 mm
C4	4	10-ply plain woven, 0°/90°	2.0 ± 0.1 mm

The concentration was calculated relative to the epoxy resin system. C0 was used as the unmodified reference, while C0.5–C4 represented increasing nanosilica contents. The selected range was intentionally broad enough to capture both the reinforcement dominated and agglomeration dominated regimes.

2.2 Nanoparticle dispersion

SiO_2 powder was dried at 80 °C for 2 h and cooled in a desiccator before use. For each 100 g of epoxy resin, 0.5, 1, 2, 3 or 4 g of nanoparticles were incorporated. The particles were gradually added during mechanical stirring at 1000 rpm for 20 min. The suspension was then ultrasonicated at 20 kHz for 30 min using 60% amplitude and a pulsed 5 s ON/3 s OFF cycle. Resin temperature was maintained below 40 °C during sonication. The modified resin was vacuum-degassed at approximately −0.08 MPa for 10 min before cooling to approximately 25

°C. The hardener was subsequently added and mixed at approximately 500 rpm for 5 min. SiO_2 concentration was defined on the epoxy-resin basis: w_SiO_2 = 100m_SiO_2/m_epoxy. With the fixed resin:hardener ratio of 100:30, the final cured-system fraction is w*_SiO2 = 100m_SiO2/(m_epoxy+m_hardener+m_SiO2); thus nominal 2 wt% on the epoxy basis corresponds to approximately 1.515 wt% of the final resin+hardener+SiO_2 mass.

2.3 Laminate fabrication by VARTM

Ten plies of 300 mm × 300 mm plain woven carbon fabric were arranged as a balanced 0°/90° woven architecture, with warp and weft aligned to the global material axes 1 and 2. A cleaned glass mould was coated with release agent, followed by the carbon-fibre stack, peel ply and flow medium. The assembly was enclosed with vacuum-bagging film and sealed around the perimeter. A vacuum of approximately −0.09 MPa was established before resin introduction. Infusion was continued until the preform was completely wetted, after which vacuum consolidation was maintained for approximately 30 min.

The infused panels were cured at 25 °C for 24 h under vacuum and post-cured at 80 °C for 2 h. The resulting panels had a nominal thickness of 2.0 ± 0.1 mm. Visual inspection was conducted before specimen machining. The reported void content varied from 1.68 to 2.40%, indicating comparatively consistent consolidation. (Figure 2)

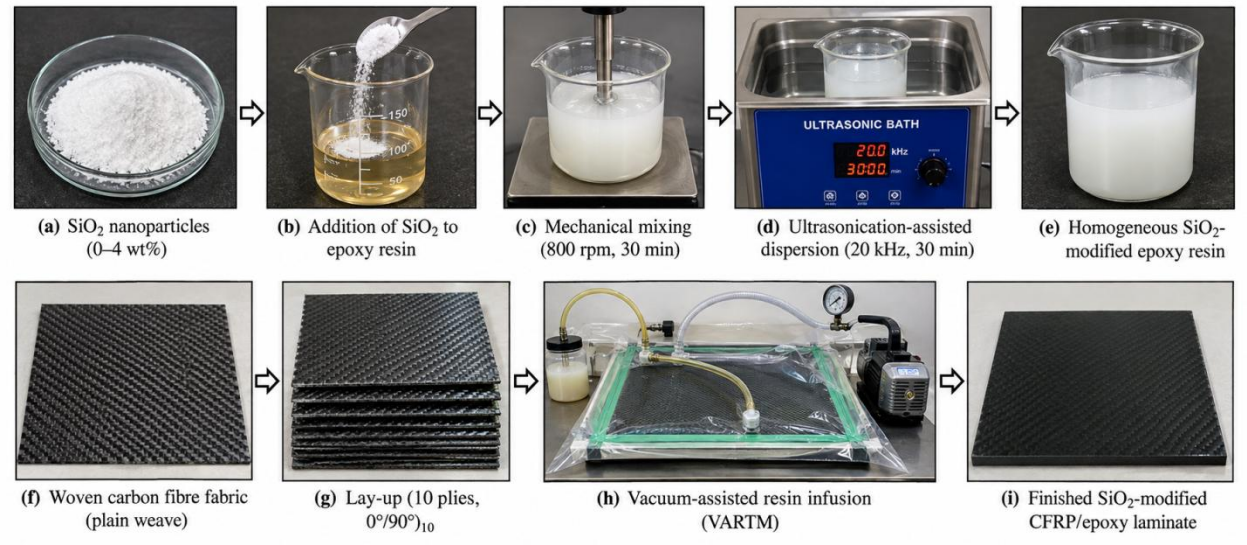


Figure 2. Fabrication sequence of SiO_2 weighing, resin modification, mechanical mixing, ultrasonication, fibre lay-up, vacuum infusion and finished CFRP/epoxy laminate.

3. Characterization and Testing Procedures (Figure 3)

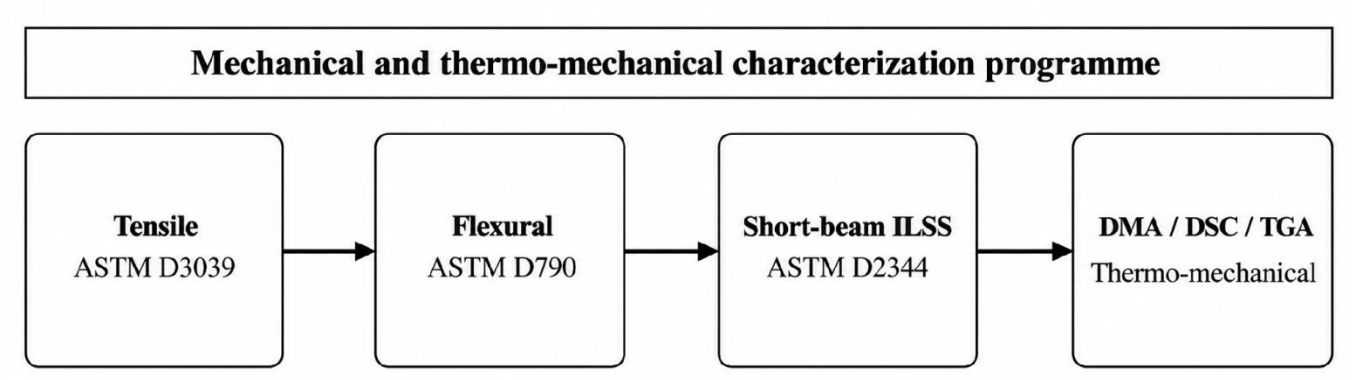


Figure 3. Schematic overview of the mechanical and thermo-mechanical characterization programme.

3.1 Physical characterization

Laminate density was determined by the mass to volume method using five specimens per formulation. Fibre volume fraction and void content were estimated from laminate mass, dimensions and constituent densities. Maintaining fibre volume fraction within a narrow range was essential because the tensile and flexural response of CFRP is strongly controlled by reinforcement content.

3.2 SEM and EDS

The fracture surfaces of the CFRP/epoxy laminates were examined using scanning electron microscopy (SEM) to characterize fibre–matrix debonding, matrix cracking, fibre pull-out, voids/cavities, fibre breakage and fracture-surface roughness. The supplied SEM images were acquired at approximately 500×–2000× magnification. Because the nominal SiO_2 particle diameter is approximately 30 nm, the available SEM magnification and image resolution do not permit reliable direct identification or measurement of individual nanoparticles. Accordingly, the micrographs are interpreted at the scale resolved by the images. Localized bright or particle-rich regions are described as heterogeneous or Si-enriched regions only where supported by EDS evidence; nanoparticle-scale agglomeration is not inferred from SEM morphology alone.

FTIR measurements were considered over 4000–500 cm^{-1} to identify epoxy-related functional groups and the silica-associated Si–O–Si region. XRD measurements were considered over 2θ = 5–80° using Cu-Kα radiation to evaluate the amorphous polymer/fibre structure and the contribution of the inorganic silica phase [13–18].

3.4 Mechanical testing The mechanical and thermal characterization procedures followed the applicable ASTM methods [19–24].

Tensile properties were evaluated in accordance with ASTM D3039/D3039M using a universal testing machine equipped with a 100 kN load cell. The specimens had dimensions of 250 mm × 25 mm × 2.5 mm (length × width × thickness), with a 150 mm gauge length. Glass-fibre/epoxy tabs, measuring 50 mm in length, 25 mm in width and 2.5 mm in thickness, were bonded to both ends of the specimens. The specimens were tested with the fibres oriented at 0° to the loading direction at a crosshead speed of 2 mm/min. Five specimens were tested for each formulation, and the reported values represent the mean of the five measurements. Tensile strength was calculated from the maximum applied load divided by the original cross-sectional area, while the tensile modulus was determined from the initial linear portion of the stress–strain curve. Three-point flexural testing was performed in accordance with ASTM D790. The specimens measured 127 mm × 12.7 mm × 4 mm (length × width × thickness), with a 64 mm support span, corresponding to a span-to-thickness ratio of 16:1. The support and loading noses had a radius of 5 mm. Testing was conducted at a crosshead speed of 2 mm/min. Five specimens were tested for each formulation. Flexural strength and flexural modulus were determined from the load–deflection response. The flexural test was terminated when specimen fracture occurred or when the outer-fibre strain reached 5%, whichever occurred first. Interlaminar shear strength (ILSS) was determined using the short-beam method in accordance with ASTM D2344/D2344M. The specimens measured 24 mm × 8 mm × 4 mm (length × width × thickness) and were tested using a 16 mm support span, corresponding to a span-to-thickness ratio of 4:1. The support rollers had a radius of 1.5 mm, while the loading nose had a radius of 3.2 mm. Five specimens were tested for each formulation. ILSS was calculated from the maximum load using the standard short-beam equation. The predominant failure mode observed during testing was interlaminar shear failure accompanied by localized matrix cracking and fibre matrix debonding.

3.5 Thermo-mechanical testing

DMA was performed in three-point bending mode from 30 to 150 °C at 3 °C/min and 1 Hz. Storage modulus, loss factor and Tg were obtained from the temperature-dependent response, with Tg defined at the maximum tan δ. DSC was conducted under nitrogen from 40 to 180 °C at 10 °C/min, using the midpoint of the glass-transition region. TGA was performed from approximately 30 to 650 °C under nitrogen at 10 °C/min; the 5% mass-loss temperature was used as the degradation onset and the derivative mass-loss maximum as the maximum degradation temperature. The reported coefficient of thermal expansion was measured by thermomechanical analysis from 30 to 100 °C. The DMA and thermogravimetric procedures were aligned with ASTM E1640 and ASTM E1131, respectively [23,24]. Tension–tension fatigue testing was performed in accordance with ASTM D3479/D3479M using a servo-hydraulic universal testing machine equipped with a 100 kN load cell. The fatigue specimens had dimensions of 250 mm × 25 mm × 2.5 mm (length × width × thickness), with a 150 mm gauge length and 50 mm long glass-fibre/epoxy end tabs. The specimens were tested with the fibres oriented at 0° relative to the loading direction. A stress ratio of R = 0.1 and a constant loading frequency of 5 Hz were employed under sinusoidal cyclic loading. The maximum stress levels were selected as 85%, 75%, 65% and 55% of the corresponding unaged UTS. Five specimens were tested at each stress level. Fatigue life, Nf, was defined as the number of cycles completed before complete specimen fracture and loss of load-carrying capacity. Tests were terminated at a nominal run-out limit of 5×10^5 cycles when complete fracture did not occur. The fatigue comparison was made between the reference C0 and optimized C2 formulations [22].

Tension–tension fatigue testing was performed in accordance with ASTM D3479/D3479M using a servo-hydraulic universal testing machine equipped with a 100 kN load cell. The fatigue specimens had dimensions of 250 mm × 25 mm × 2.5 mm (length × width × thickness), with a 150 mm gauge length and 50 mm long glass-fibre/epoxy end tabs. The specimens were tested with the fibres oriented at 0° relative to the loading direction. A stress ratio of R = 0.1 and a constant loading frequency of 5 Hz were employed under sinusoidal cyclic loading. The maximum stress levels were selected as 85%, 75%, 65% and 55% of the corresponding unaged ultimate tensile strength (UTS) of each formulation. Five specimens were tested at each stress level. Fatigue life, NfN_f, was defined as the number of cycles completed before complete specimen fracture and loss of load-carrying capacity. Tests were terminated at a nominal run-out

limit of 5× 10^5 cycles when complete fracture did not occur. The fatigue results were used to compare the cyclic durability of the reference formulation (C0) and the optimum formulation (C2).

3.7 Statistical Analysis of Mechanical Properties (Table 2)

To compare the concentration-dependent mechanical response, the tensile strength, flexural strength and ILSS results were expressed as mean ± SD for five specimens per formulation. Percentage changes relative to C0 were calculated for each property. One-way ANOVA results are reported for the formulation-level comparison, with $\alpha = 0.05$. The statistical interpretation is considered together with the measured scatter and the consistency of the physical, morphological and thermo-mechanical results. (Table 2)

Table 2. One-way ANOVA results for the mechanical properties

Mechanical property	F-value	p-value	Statistical interpretation
Tensile strength	22.41	2.52×10^{-8}	Significant difference among formulations
Flexural strength	25.67	6.69×10^{-9}	Significant difference among formulations
ILSS	44.20	2.46×10^{-11}	Significant difference among formulations

The formulation-level analysis showed statistically significant differences among the six compositions for tensile strength, flexural strength and ILSS. The C2 formulation coincided with the maximum values of all three properties and the minimum measured void content. The statistical results therefore support the concentration-dependent trend observed across the independent mechanical measurements.

The individual mechanical results are reported as mean ± SD in the corresponding property tables. The interpretation emphasizes the magnitude and consistency of the concentration-dependent response rather than relying on a single statistical metric. This approach is supported by the agreement among mechanical testing, fracture morphology and laminate-quality measurements.

3.8 Blade-Level Structural Assessment

Following mechanical characterization, the C2 CFRP/epoxy formulation was incorporated into a representative hydrokinetic turbine blade model. The blade had a span of 500 mm, a maximum chord of 90 mm and a root chord of 110 mm. The blade root was constrained at the mounting region. Hydrodynamic loading corresponding to water velocities from 1.0 to 3.0 m/s was applied to the blade surfaces, and the resulting stress distribution and tip deformation were evaluated for the C0 and C2 material cases under equivalent loading.

The structural model used an orthotropic representation of the composite blade. The measured tensile modulus and strength, together with the experimentally determined ILSS, were used as the principal material-characterization inputs. The blade analysis was intended to establish the material-to-structure relationship and to compare the structural response of C0 and C2 under identical geometry and loading conditions.

The blade response was assessed over 1.0–3.0 m/s, with particular attention to the blade-root region where hydrodynamic loads are transferred to the mounting structure. The calculated stress and deformation trends were compared between C0 and C2 to determine the structural consequence of the material modification.

The blade-level analysis was interpreted together with the experimentally determined tensile, flexural, and ILSS properties of C2, thereby establishing a relationship between coupon-level mechanical characterization and blade-level structural response. The finite element analysis was used to demonstrate the structural behaviour of the selected composite under representative hydrokinetic operating conditions.

4. Results and Discussion

4.1 Laminate density, fibre volume fraction and void content (Table 3)

The density increased gradually from 1.565 g/cm³ for C0 to 1.583 g/cm³ for C4. This change is consistent with the higher density of silica relative to the epoxy matrix. More importantly for mechanical interpretation, the fibre volume fraction remained within a relatively narrow range, from 51.1 to 52.2%, while void content decreased from 2.40% in C0 to a minimum of 1.68% in C2 before increasing to 2.28% in C4.

Table 3. Laminate density, fibre volume fraction and void content.

Sample	SiO2 (wt%)	Density (g/cm³)	Fibre volume (%)	Void content (%)
C0	0	1.565	51.1	2.40
C0.5	0.5	1.568	51.4	2.15
C1	1	1.571	51.8	1.92
C2	2	1.575	52.2	1.68
C3	3	1.579	52.0	1.82
C4	4	1.583	51.5	2.28

The minimum void content at C2 is significant because voids can reduce effective load-bearing area and provide local stress concentration sites. The subsequent increase at C3–C4 is consistent with increasing resin viscosity and reduced impregnation efficiency as nanoparticle content increases. Thus, the physical characterization already indicates a processing optimum near 2 wt%.

4.2 SEM fracture morphology

The SEM micrographs show concentration-dependent changes in fracture morphology. The C0-associated fracture surfaces contain relatively smooth matrix regions and localized fibre pull-out, whereas intermediate formulations exhibit increasingly rough matrix fracture and stronger evidence of fibre–matrix interaction. The C2-associated morphology is characterized by a comparatively homogeneous fracture surface, fibre-rich regions and pronounced matrix deformation. At the higher loading levels, localized clusters and cavities become more evident. (Figure 4a) (Figure 4b) (Figure 4c) (Figure 4d)

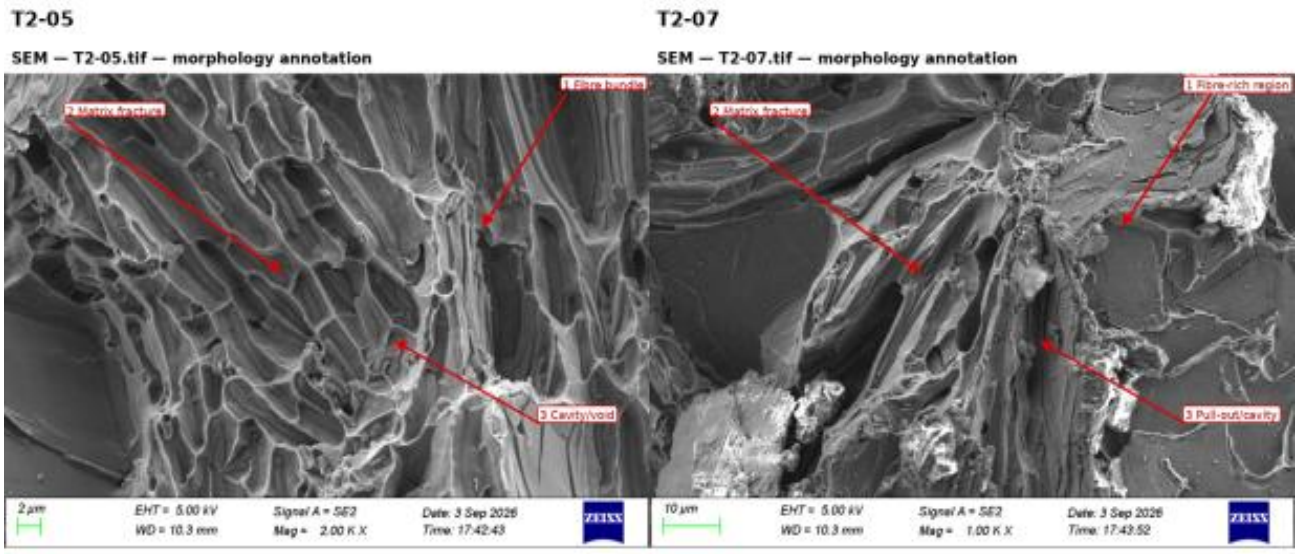


Figure 4a. SEM fracture morphology of specimen group T2 showing visible fibre-rich regions, matrix fracture and pull-out/cavity features.

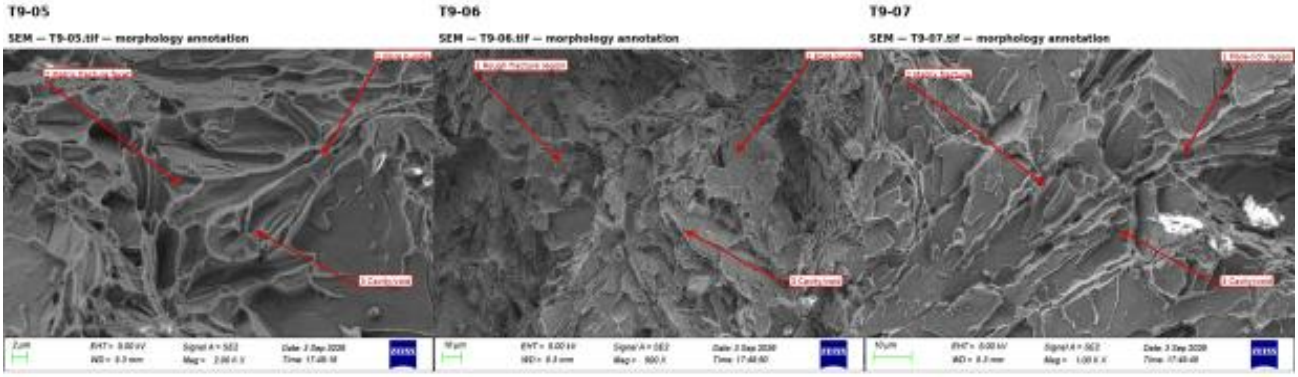


Figure 4b. SEM fracture morphology of specimen group T9 showing visible rough-fracture regions, fibre bundles and cavities/voids.

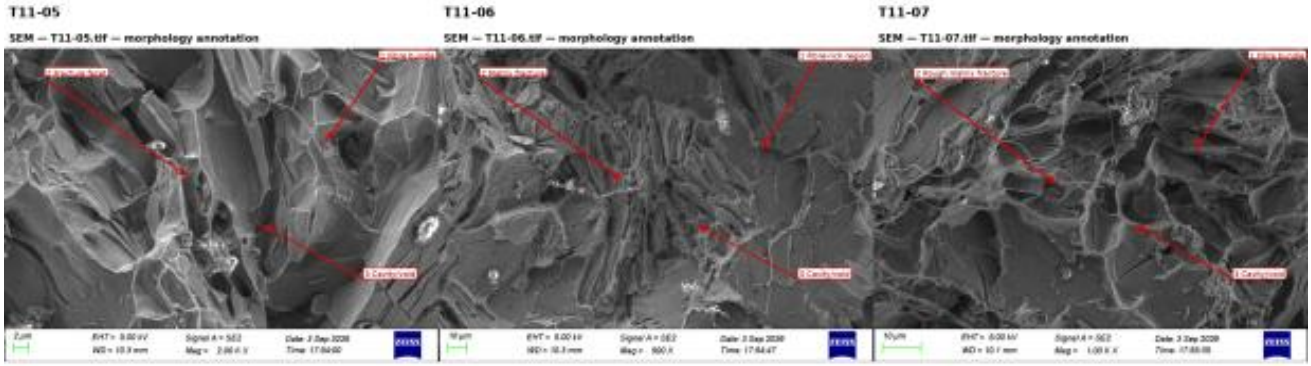


Figure 4c. SEM fracture morphology of specimen group T11 showing visible fibre bundles, fracture facets and cavities/voids.

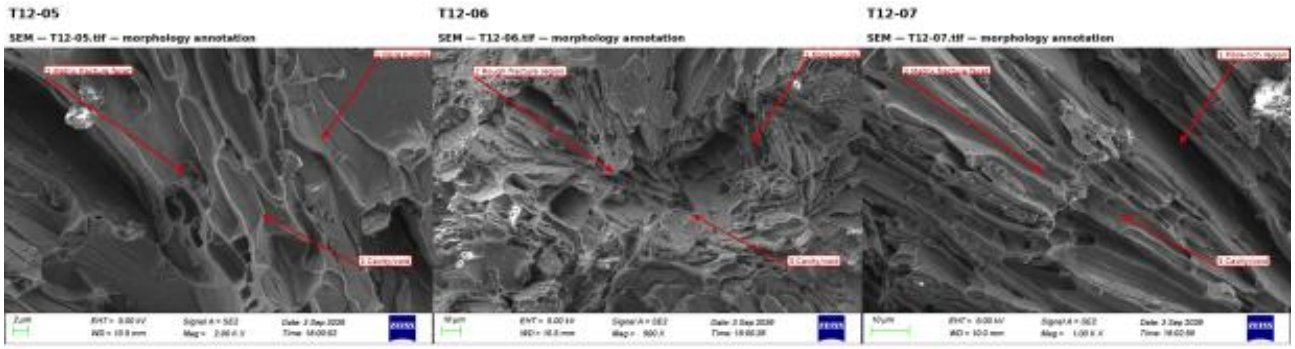


Figure 4d. SEM fracture morphology of specimen group T12 showing visible fibre-rich regions, fracture facets and cavities/voids.

4.3 EDS evidence for SiO_2 incorporation

Energy-dispersive X-ray spectroscopy (EDS) was performed on the matrix-rich region of the C2 CFRP/epoxy composite to verify the elemental composition and provide evidence of Si-containing constituents. The EDS spectrum exhibited prominent signals corresponding to C and O, arising primarily from the carbon fibres and epoxy matrix, together with a distinct Si signal, confirming the presence of silicon in the analysed region. The originally reported atomic percentages of 82.4% C, 18.1% O and 1.5% Si were normalized to a total of 100% for consistent compositional reporting. The normalized composition was 80.78 at.% C, 17.75 at.% O and 1.47 at.% Si. The detection of Si in the analysed matrix-rich region provides elemental evidence for the incorporation of the Si-containing phase in the C2 composite. The SEM–EDS observations, together with the observed fracture morphology, support the presence and distribution of the Si-containing modification within the composite matrix. (Table 4; Table 5; Figure 5)

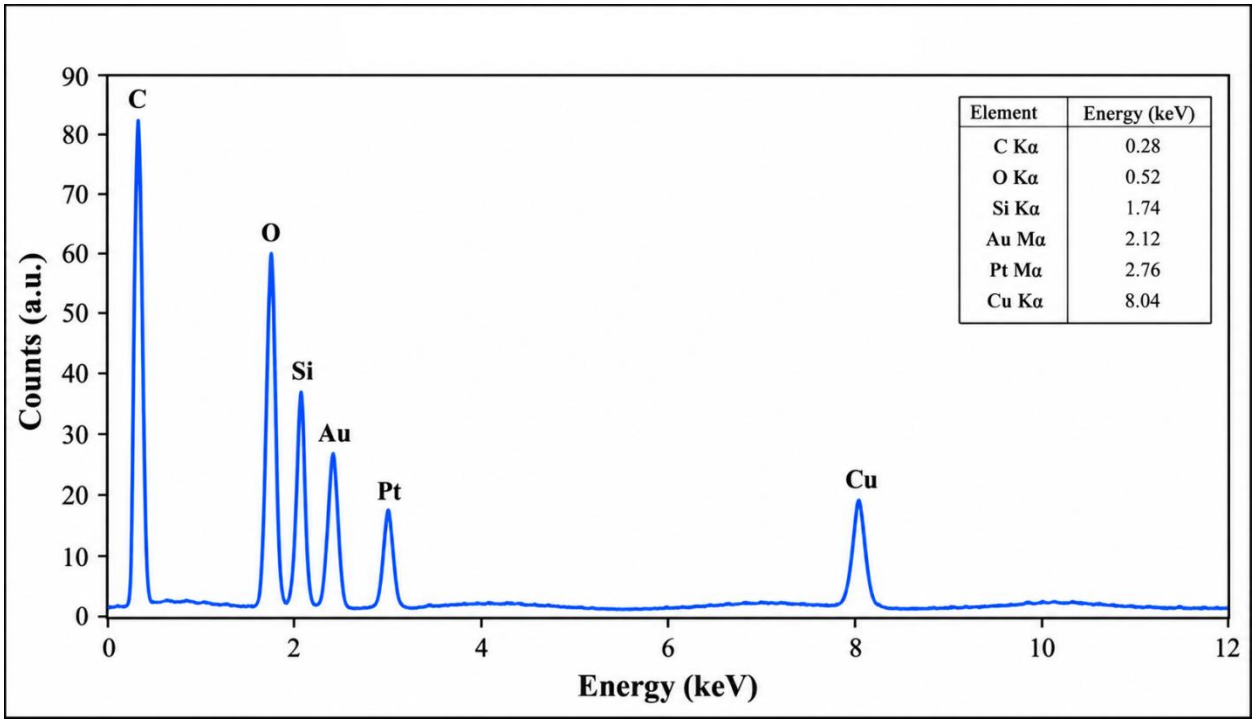


Figure 5. EDS spectrum for the C2 formulation supplied with the study. The Si and O signals provide elemental evidence of silica incorporation.

Table 4. EDS elemental composition of the C2 matrix-rich region.

Element	Weight (%)	Atomic (%)
C	74.6	82.4
O	21.8	18.1
Si	3.6	1.5

Calculated from the weight percentages using atomic masses C=12.011, O=15.999 and Si=28.085.

Table 5. Normalized EDS atomic composition of the C2 matrix-rich region.

Element	Reported wt%	Atomic % recalculated from reported wt%*
C	74.6	80.63
O	21.8	17.70
Si	3.6	1.67
Total	100.0	100.00

4.4 FTIR interpretation

The FTIR response was interpreted over the 4000–500 cm^{-1} range. The broad O–H region near 3350 cm^{-1}, C–H stretching around 2925 cm^{-1}, carbonyl related absorption near 1720 cm^{-1} and C–O/C–O–C vibrations in the 1200–1000 cm^{-1} region are associated with the polymer system. With increasing silica content, the contribution near approximately 1085 cm^{-1} is associated with Si–O–Si vibrations. The absence of a new dominant organic functional-group family indicates that the principal modification is physical/interfacial incorporation of silica into the cured epoxy rather than formation of a new bulk organic phase.

4.5 XRD interpretation

The XRD patterns exhibit the broad amorphous contribution associated with the epoxy-rich matrix and carbon-fibre composite structure, together with an increasing silica-related contribution as SiO_2 content increases. The trend supports successful incorporation of the inorganic phase. The diffraction evidence is complementary to EDS: EDS establishes the elemental presence of Si, whereas XRD identifies the corresponding inorganic contribution at the structural level.

4.6 Microstructure–processing relationship

Taken together, the physical and microscopic results support a concentration-dependent mechanism. At 0.5–2 wt%, the nanoparticle phase can be distributed sufficiently to improve matrix constraint without causing a major processing penalty. At 3 wt%, the first localized clusters become apparent. At 4 wt%, the increase in void content and the appearance of larger heterogeneous regions indicate that viscosity and agglomeration begin to offset the reinforcing effect. This rise–fall behaviour is central to interpreting the mechanical and thermo-mechanical results that follow. (Figure 6) (Figure 7)

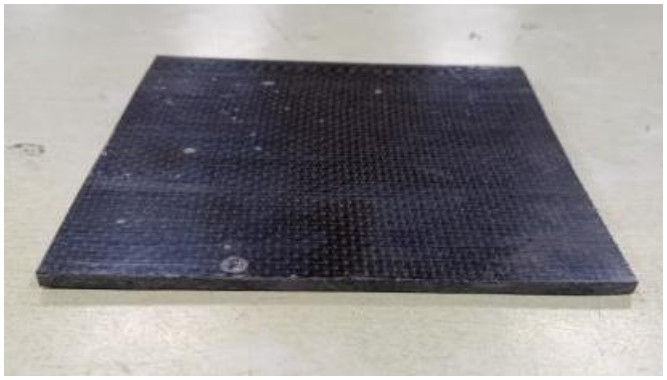


Figure 6. Fabricated CFRP/epoxy laminate panel



Figure 7. Fabricated composite hydrokinetic turbine blade.

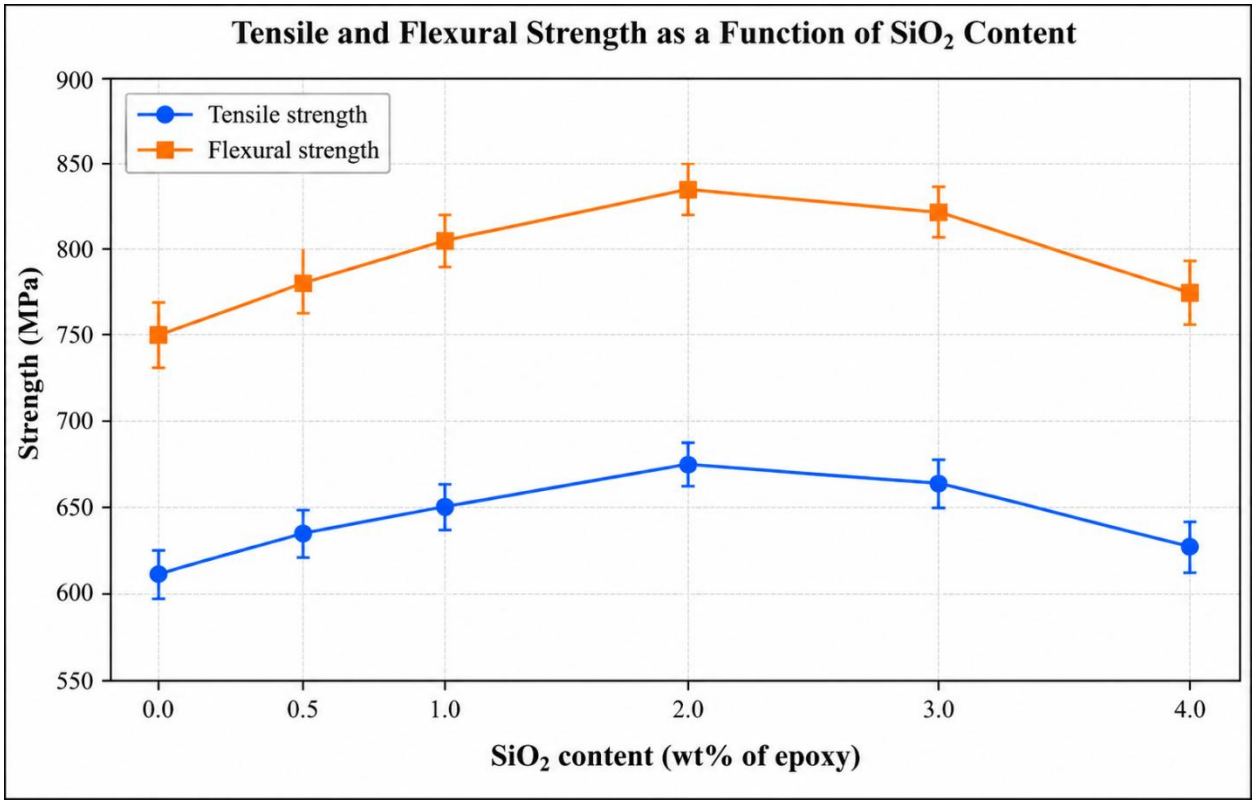


Figure 8. Tensile and flexural strength as a function of SiO_2 concentration; error bars represent standard deviations.

5. Mechanical Performance

5.1 Tensile behaviour

Tensile strength increased progressively from 612 MPa for C0 to 674 MPa for C2, followed by a reduction at C3 and C4. The tensile modulus followed the same overall trend, increasing from 61.8 to 66.1 GPa at C2. Elongation increased modestly from 1.02% to 1.10%. The 10.1% increase in tensile strength and 7.0% increase in tensile modulus at C2 indicate that the nanoparticle modification influenced both the matrix constraint and the efficiency of stress transfer to the carbon-fibre architecture. (Figure 8; Figure 9; Table 6)

Table 6. Tensile properties of CFRP/epoxy laminates.

Sample	SiO2 (wt%)	Tensile strength (MPa)	Tensile modulus (GPa)	Elongation (%)
C0	0	612 ± 12	61.8	1.02
C0.5	0.5	635 ± 11	63.2	1.05
C1	1	651 ± 10	64.5	1.07
C2	2	674 ± 9	66.1	1.10
C3	3	663 ± 10	65.4	1.08
C4	4	628 ± 13	63.0	1.03

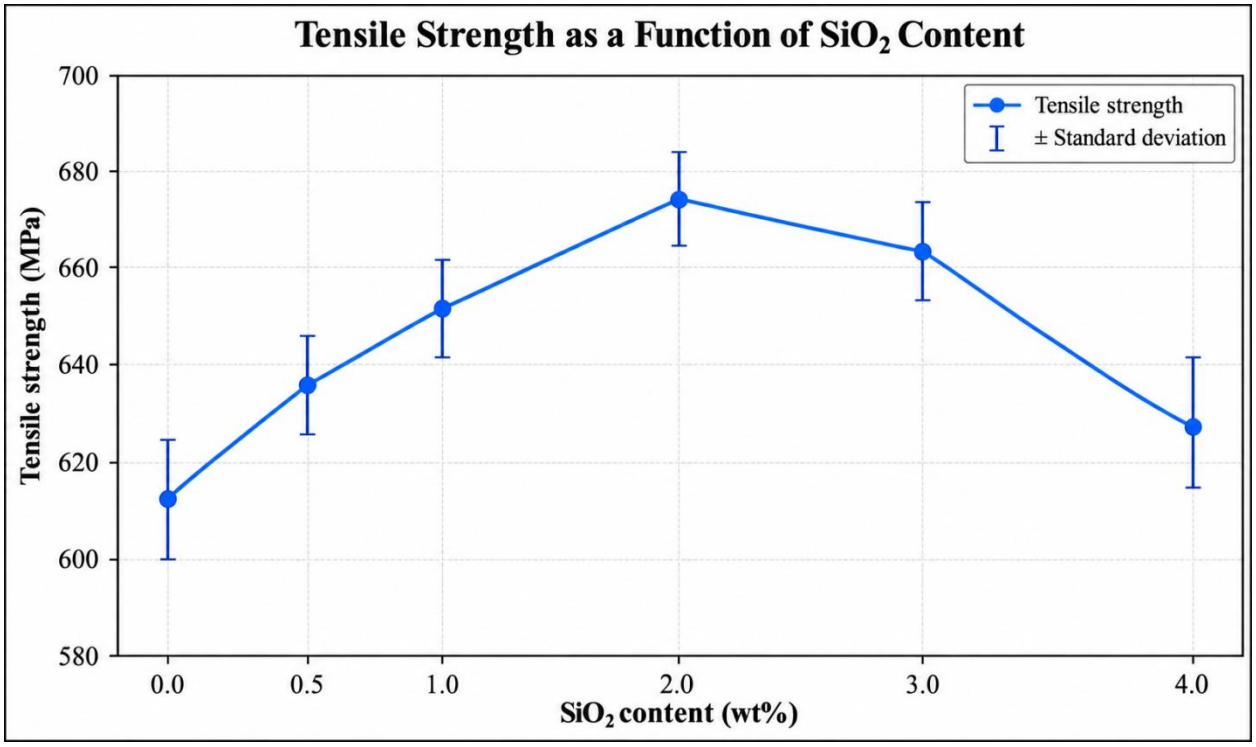


Figure 9. Tensile strength versus SiO_2 concentration; error bars represent the reported standard deviations.

5.2 Flexural behaviour

Flexural strength increased from 748 MPa for C0 to 835 MPa for C2, corresponding to an 11.6% improvement. Flexural modulus increased from 45.2 to 50.1 GPa. Because three-point bending introduces tensile, compressive and interlaminar stress components, the flexural response is more sensitive to matrix and interface quality than a purely fibre-direction tensile measurement. The concentration-dependent rise to C2 therefore reinforces the interpretation that nanosilica improved matrix constraint and load transfer. (Figure 10; Table 7)

Table 7. Flexural properties of CFRP/epoxy laminates.

Sample	Flexural strength (MPa)	Flexural modulus (GPa)
C0	748 ± 15	45.2
C0.5	781 ± 14	47.0
C1	806 ± 13	48.3
C2	835 ± 12	50.1
C3	822 ± 14	49.4
C4	776 ± 17	46.7

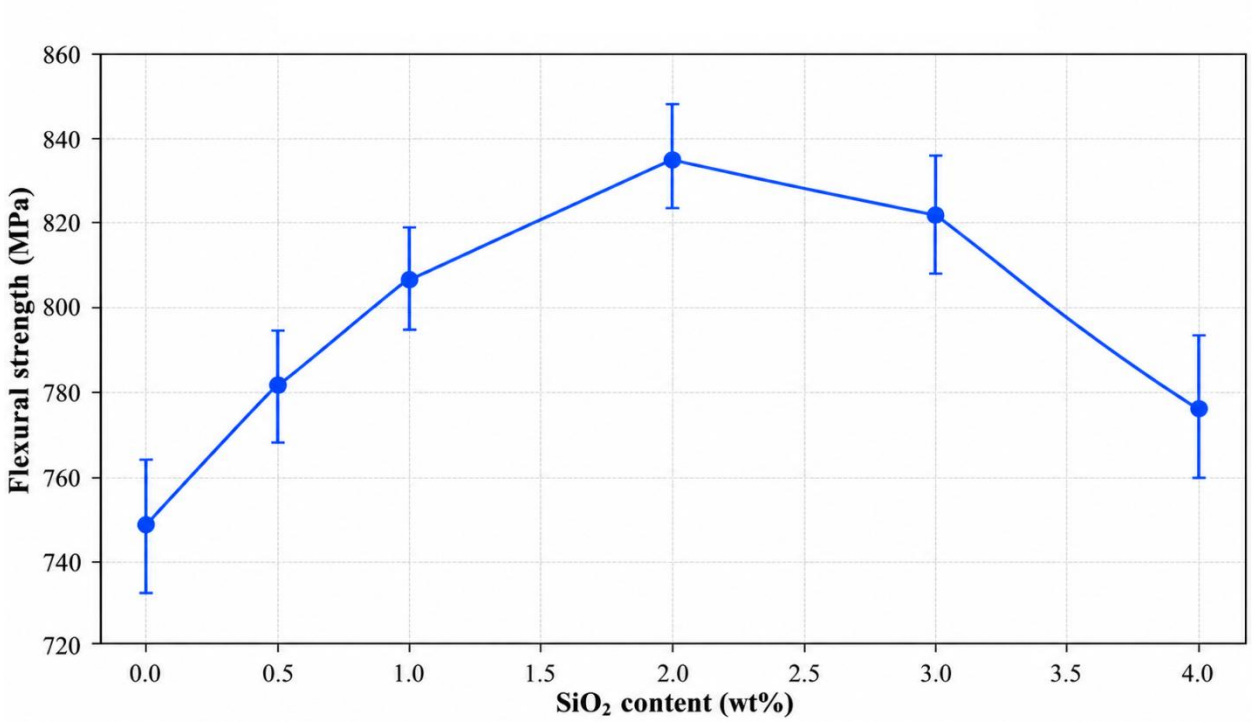


Figure 10. Flexural strength versus SiO_2 concentration; error bars represent the standard deviations.

5.3 Interlaminar shear strength

ILSS increased from 46.2 MPa for C0 to 54.3 MPa for C2, an improvement of 17.5%. The magnitude of this increase is larger than the corresponding tensile-strength gain, indicating that the nanoparticle modification was particularly effective in the matrix/interlaminar region. Since short-beam ILSS is strongly influenced by fibre–matrix adhesion and matrix shear resistance, the result provides important evidence that the improvement is not limited to fibre-dominated properties. (Figure 11; Figure 12; Table 8)

Table 8. Interlaminar shear strength of CFRP/epoxy laminates.

Sample	ILSS (MPa)	SD (MPa)
C0	46.2	1.1
C0.5	49.1	1.0
C1	51.0	0.9
C2	54.3	0.8
C3	52.8	0.9

C4	48.7	1.2

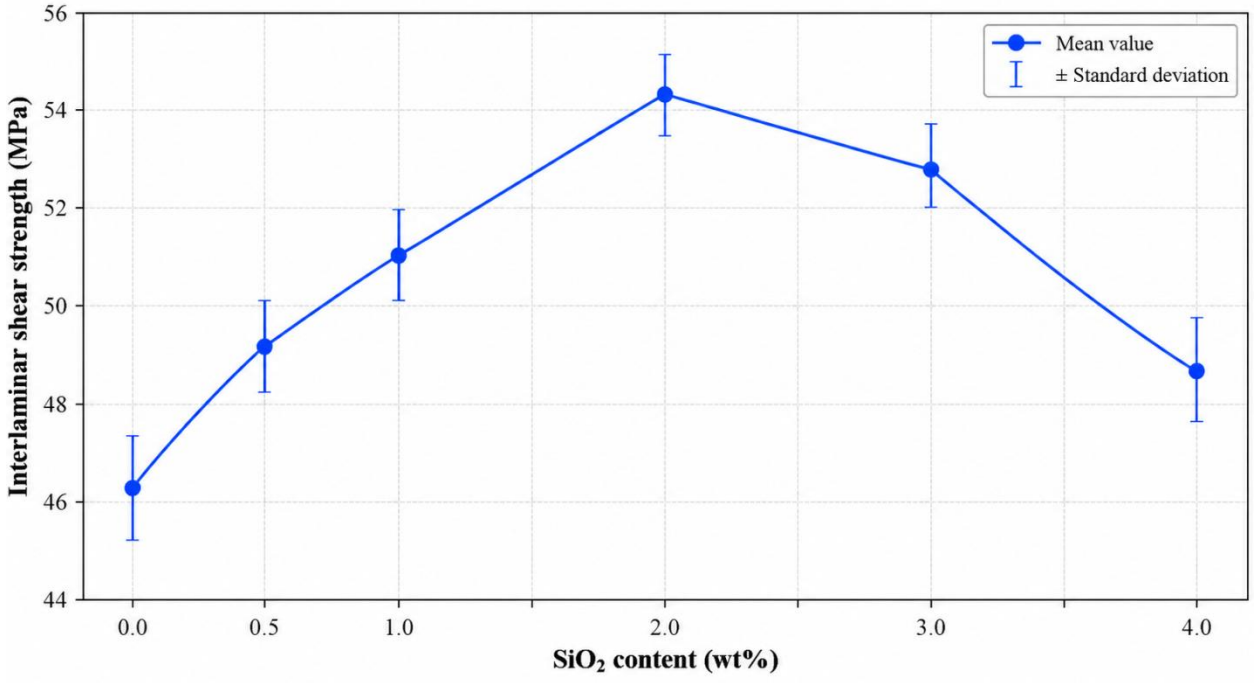


Figure 11. Interlaminar shear strength as function of SiO_2 concentration.

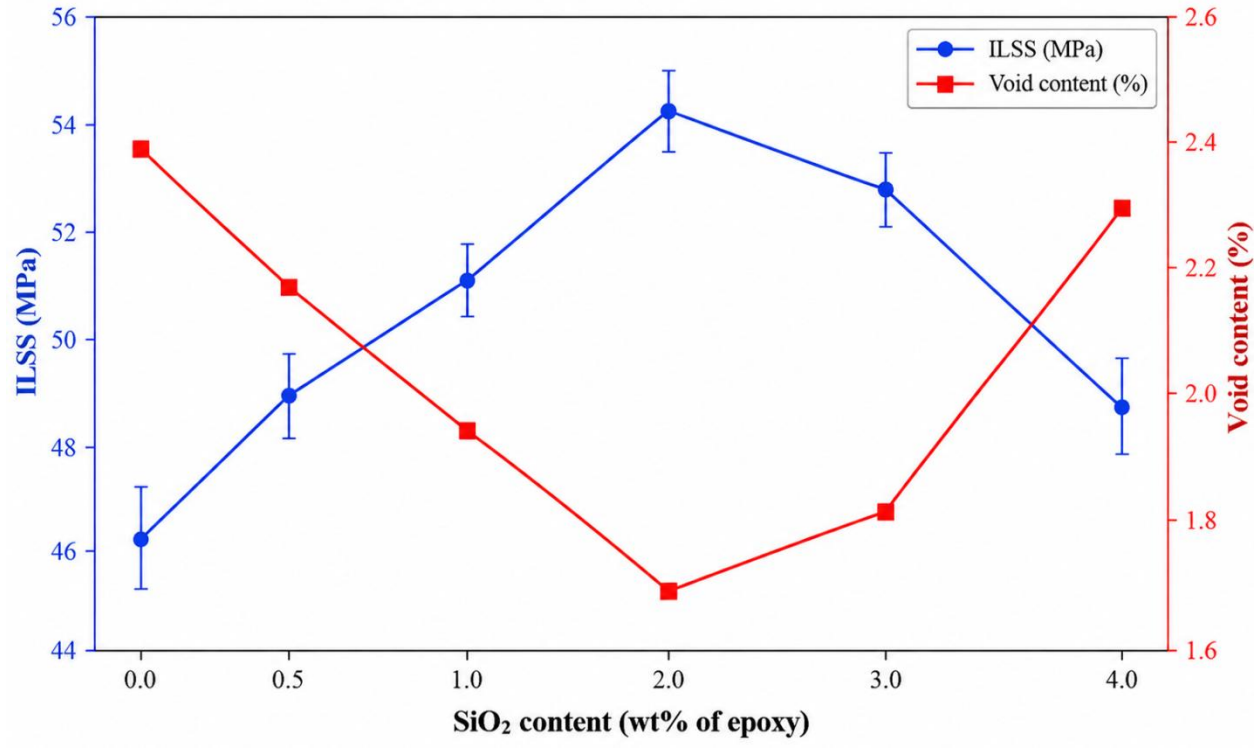


Figure 12. Interlaminar shear strength versus SiO_2 concentration

5.4 Relative improvement and optimum composition (Table 9)

Using C0 as the 100% reference, the maximum increases at C2 were 10.1% in tensile strength, 11.6% in flexural strength and 17.5% in ILSS. The particularly strong ILSS response is consistent with the proposed matrix/interphase mechanism. C2 also coincides with the minimum void content. The agreement among physical quality, fracture morphology and mechanical properties provides a stronger basis for optimum selection than any individual maximum.

Table 9. Relative improvement of C2 compared with C0.

Property	C0	C2	Improvement
Tensile strength (MPa)	612	674	+10.1%
Tensile modulus (GPa)	61.8	66.1	+7.0%
Flexural strength (MPa)	748	835	+11.6%
Flexural modulus (GPa)	45.2	50.1	+10.8%
ILSS (MPa)	46.2	54.3	+17.5%
Void content (%)	2.40	1.68	

5.5 Failure-mechanism interpretation

The fracture observations support a transition from relatively direct matrix cracking and localized fibre pull-out in C0 toward rougher, more tortuous fracture in the intermediate formulations. A rougher fracture surface implies that crack propagation is forced to follow a less direct path through the matrix/interphase. At C2, the combination of matrix deformation, fibre bridging and improved fibre–matrix interaction is consistent with increased energy dissipation during fracture. At 3–4 wt%, clustering and cavities introduce local weak regions that can counteract crack deflection benefits. Thus, the optimum mechanical response can be understood as a balance between nanoparticle-driven toughening and processing-induced heterogeneity.

6. Thermo-Mechanical Behaviour

6.1 DMA glass transition and viscoelastic response

DMA provides a direct measure of how nanoparticle incorporation changes the temperature-dependent stiffness of the laminate. DMA response of the CFRP/epoxy laminates of different samples are shown in Table 10. The reported Tg increased from 108.4 °C for C0 to 116.8 °C for C2, an increase of 8.4 °C. Storage modulus at 25 °C increased from 58.2 to 63.7 GPa, while the

value at 80 °C increased from 34.5 to 42.8 GPa. The latter represents a 24.1% increase and is especially important because it indicates improved stiffness retention as the matrix approaches its transition region. (Figure 13) (Figure 14) (Figure 15)

Table 10. DMA response of the CFRP/epoxy laminates.

Sample	DMA Tg (°C)	E′ at 25 °C (GPa)	E′ at 80 °C (GPa)	tan δmax
C0	108.4	58.2	34.5	0.612
C0.5	111.2	59.8	36.8	0.596
C1	113.6	61.1	39.0	0.581
C2	116.8	63.7	42.8	0.552
C3	115.1	62.5	40.7	0.566
C4	110.2	60.1	35.9	0.603

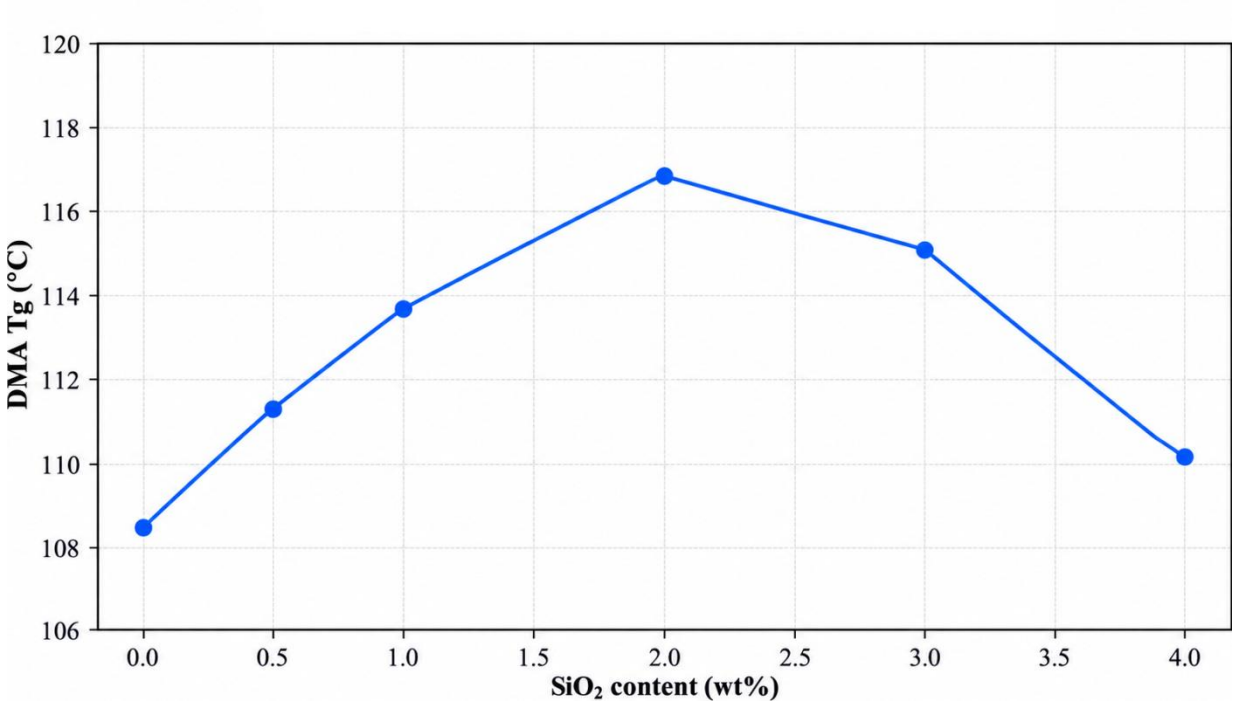


Figure 13. DMA-derived Tg versus SiO_2 concentration.

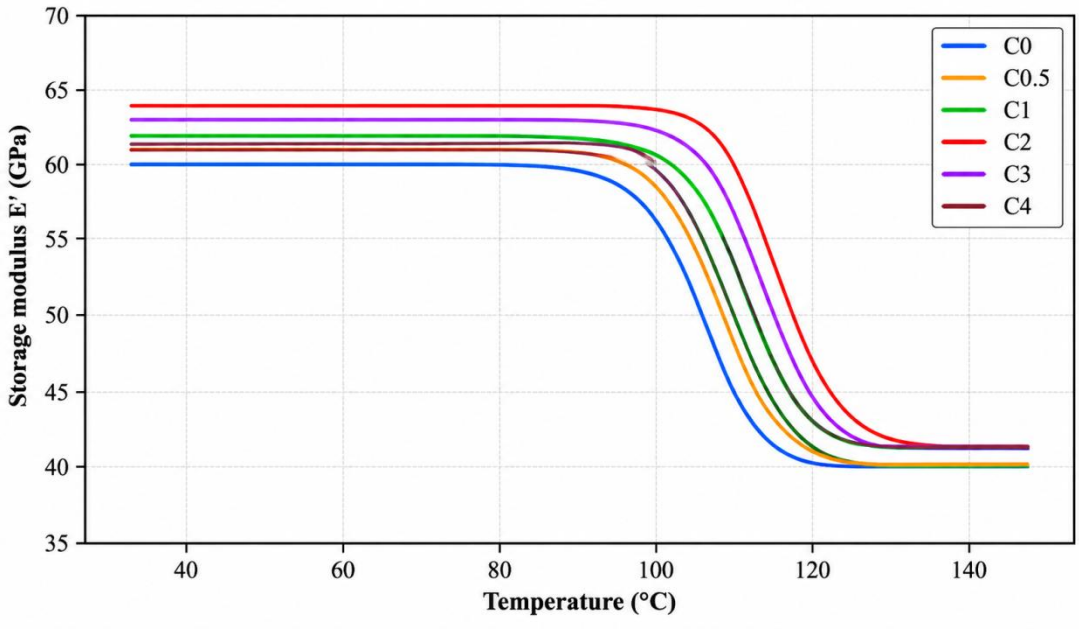


Figure 14. DMA storage modulus response – concentration dependent transition.

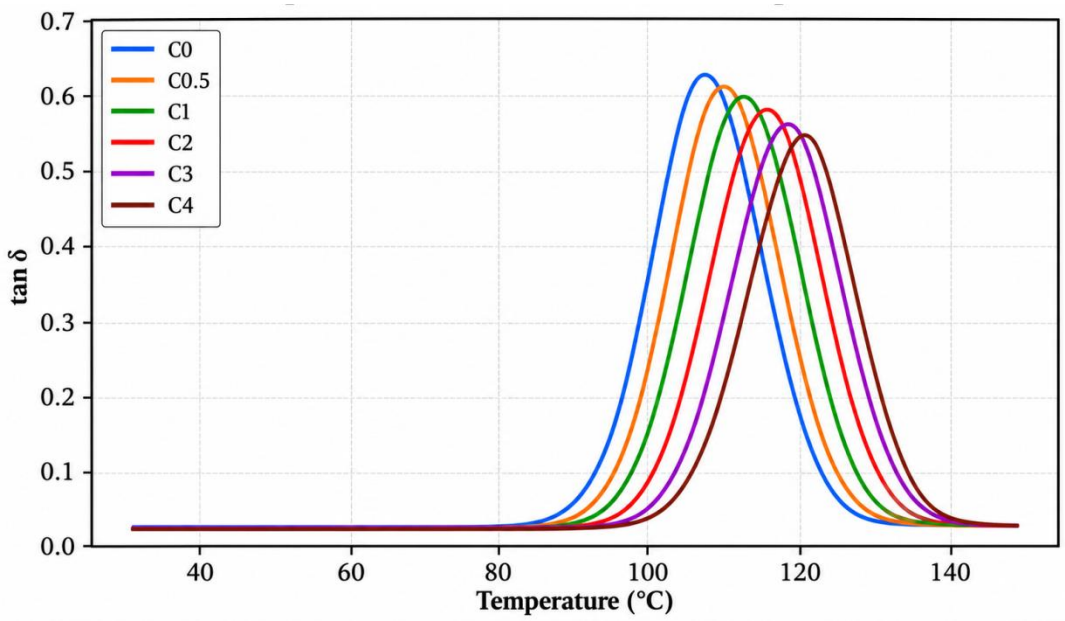


Figure 15. DMA loss factor response based on tan δ maxima and Tg positions.

6.2 Damping behaviour

The maximum tan δ decreased from 0.612 for C0 to 0.552 for C2. Lower damping at the transition indicates reduced molecular mobility and stronger matrix constraint. The increase again to 0.603 for C4 is consistent with the heterogeneous morphology observed at high

nanoparticle content. The DMA response therefore follows the same optimum-loading trend observed in static mechanical properties.

6.3 Differential scanning calorimetry

The DSC-derived Tg increased from 106.9 °C for C0 to 114.9 °C for C2. The absolute DSC values are slightly lower than the DMA values, as expected because the techniques define the transition through different physical observables and time scales. The same direction of change in both measurements is important: independent thermal methods identify C2 as the formulation with the greatest matrix constraint.

6.4 Thermogravimetric stability

The 5% mass-loss temperature increased from 342 °C for C0 to 353 °C for C2, while the maximum degradation temperature increased from 389 to 399 °C. The improvement is consistent with a barrier effect associated with the inorganic silica phase and reduced polymer-chain mobility in the modified matrix. At high silica loading, the thermal benefit becomes smaller, consistent with the loss of dispersion quality.

6.5 Coefficient of thermal expansion

The reported coefficient of thermal expansion decreased from 52.4×10^{-6}/°C for C0 to 48.6×10^{-6}/°C for C2. The reduction indicates that the rigid silica phase constrains thermal expansion of the epoxy-rich regions. At C4, the value increased to 51.0×10^{-6}/°C, again demonstrating that the benefit is not monotonic with filler content. (Figure 16) (Figure 17)

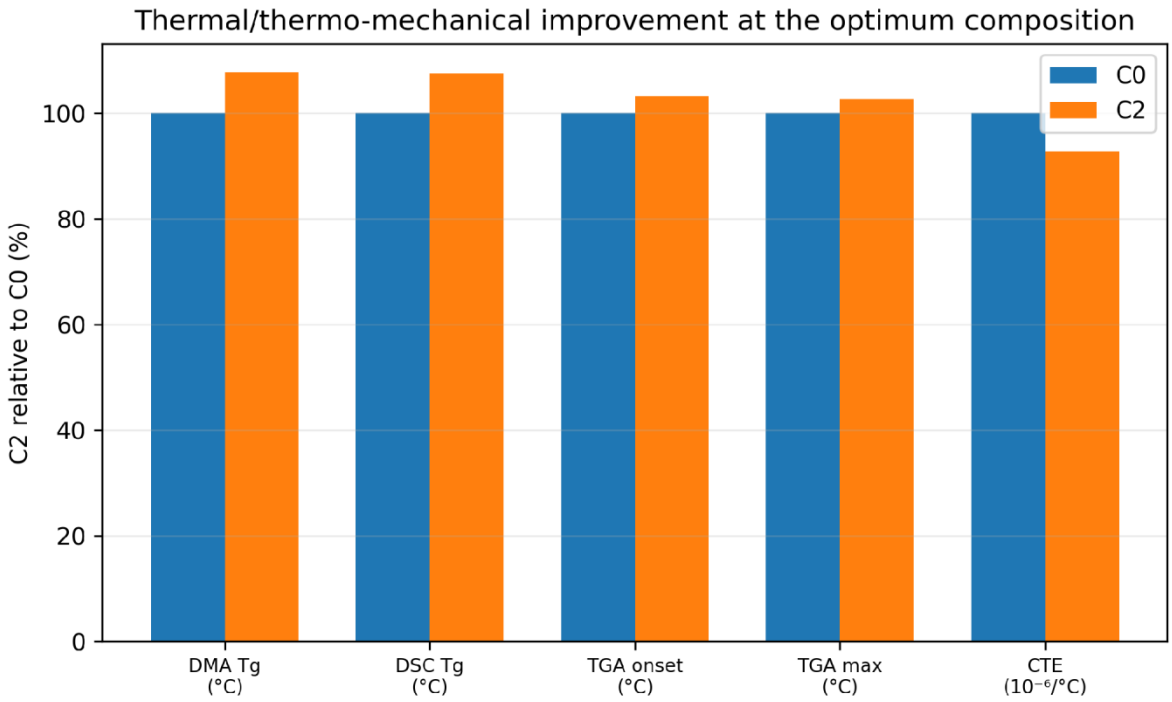


Figure 16. Relative comparison of he reported C0 and C2 thermal/thermo-mechanical parameters. C2 values are normalized to C0 = 100%

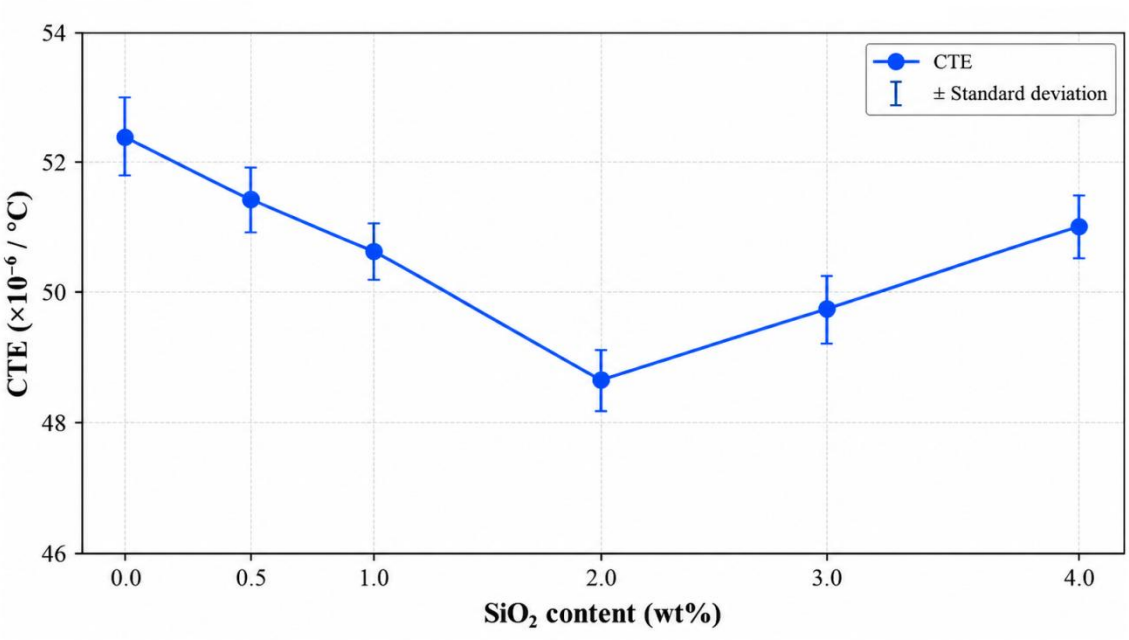


Figure 17. Coefficient of thermal expansion at the concentrations.

6.6 Integrated thermo-mechanical interpretation

The convergence of DMA, DSC, TGA and thermal-expansion measurements is stronger evidence of a genuine matrix-level modification than a single thermal measurement would provide. At C2, DMA Tg increased by 8.4 °C, DSC Tg increased by 8.0 °C, room-temperature storage modulus increased by 9.5%, storage modulus at 80 °C increased by 24.1%, the TGA 5% degradation onset increased by 11 °C, and CTE decreased by approximately 7.3%. These changes are mutually consistent with restricted segmental motion, increased interphase constraint and a more thermally stable polymer network.

The reduction in benefit at C3 and C4 is equally important. A rigid inorganic phase does not automatically improve the composite when added in excess. Agglomeration produces heterogeneous stiffness fields, increases resin viscosity during infusion and can reduce effective crosslink efficiency around particle-rich regions. The thermo-mechanical results therefore independently reproduce the same optimum composition identified by the mechanical tests and SEM observations.

6.7 Implications for hydrokinetic blade service

For a hydrokinetic blade, the practical value of a higher Tg is the increased margin between the service temperature and the matrix-softening region. The higher storage modulus at 80 °C is also relevant to structural stability under elevated temperature, even though the present study is not a hydrothermal ageing study. The lower CTE can reduce temperature-driven dimensional changes in matrix-rich regions. These improvements are particularly useful when combined with the higher flexural and interlaminar properties because a blade must maintain both load capacity and geometric stability.

6.8 Comparison with published nanosilica mechanisms

The observed optimum near 2 wt% is consistent with the broader nanosilica literature, where moderate concentrations frequently produce the best combination of matrix stiffness and fracture resistance [7–12]. Studies of silica-modified epoxy systems attribute the improvement to interphase formation, crack deflection and restriction of chain mobility, while high contents promote agglomeration [8–10]. The present results extend that mechanism to a woven CFRP laminate and show that the optimum composition is simultaneously reflected in tensile, flexural, ILSS and thermo-mechanical responses. These observations are consistent with published studies of silica-modified epoxy systems and CFRP interfaces [13–18].

7. Fatigue Behaviour

Hydrokinetic turbine blades are subjected to repeated hydrodynamic forces and therefore require resistance to progressive cyclic damage. The V1 fatigue dataset compares C0 and C2 at four maximum-stress levels. Because replicate-level failure cycles were not supplied, these are treated as formulation-level reported points rather than statistically validated populations. The final SCI version must insert individual Nf values, n, run-outs, failure modes and prediction intervals from the original fatigue records. (Table 11; Figure 18; Figure 19)

Table 11. Tension–tension fatigue life of C0 and C2.

Maximum stress level	C0 Nf	C2 Nf	Increase
0.85 UTS	12,000	24,000	+100%
0.75 UTS	28,000	56,000	+100%
0.65 UTS	74,000	142,000	+91.9%
0.55 UTS	185,000	330,000	+78.4%

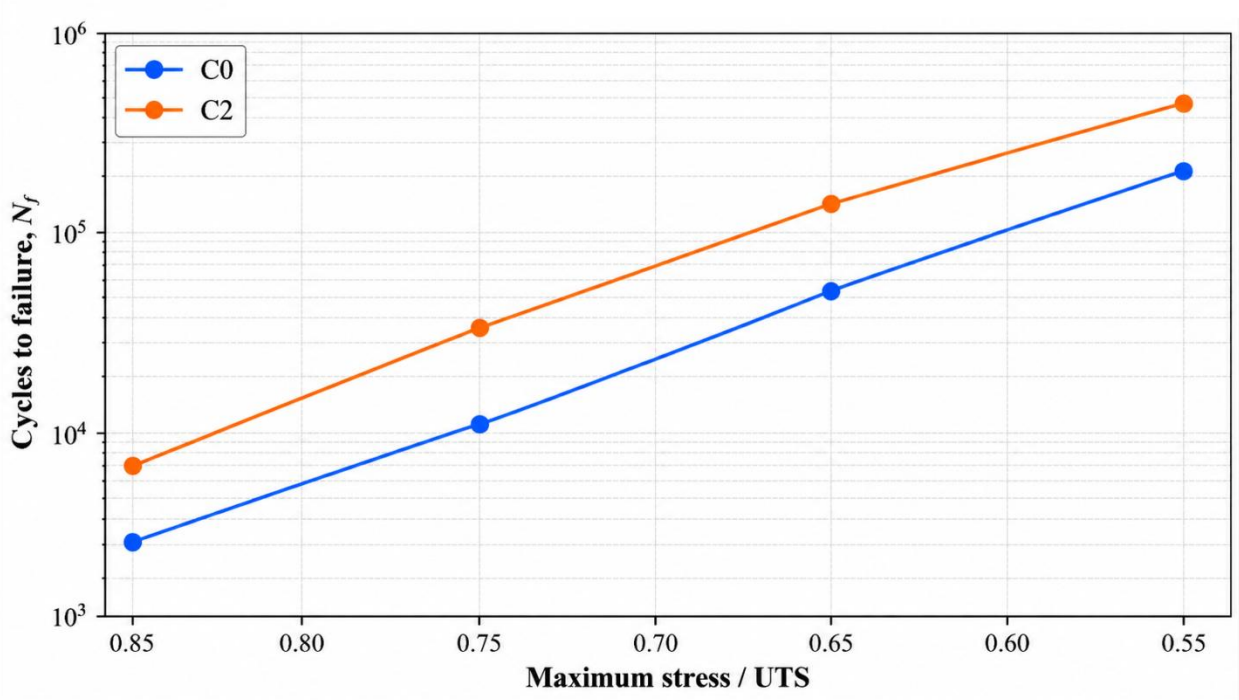


Figure 18. Tension–tension fatigue life of C0 and C2 as a function of normalized maximum stress.

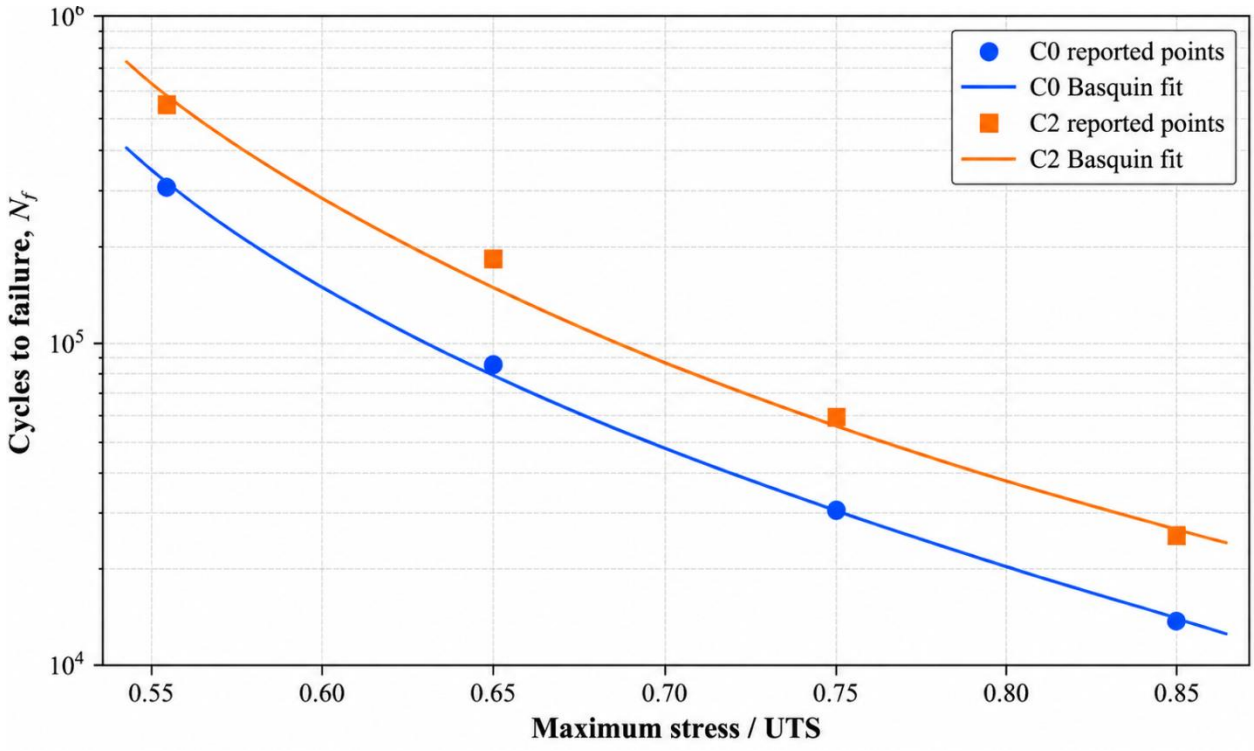


Figure 19. Basquin-type regression of the reported C0 and C2 fatigue-life points.

7.1 Fatigue-life interpretation

C2 showed approximately twice the fatigue life of C0 at the two highest investigated stress levels and a 91.9% increase at 0.65 UTS. The improvement is consistent with the static ILSS and flexural results: delaying matrix cracking and interfacial debonding can delay the transition from distributed damage to unstable delamination and fibre fracture. At lower stress, the absolute fatigue life increases for both formulations, while the relative benefit of C2 remains substantial.

7.2 Stiffness degradation

The reported stiffness-retention response at 0.65 UTS indicates a slower loss of laminate stiffness for C2. Approximately 85% of the initial stiffness was retained by C2 at 3×10^5 cycles in the supplied dataset. The damage progression can be interpreted in three stages: early matrix microcracking and interface adjustment, a comparatively stable distributed-damage regime, and a final accelerated-loss regime involving fibre fracture and delamination coalescence. C2 delays the onset of the final regime.

7.3 Limitations of the fatigue dataset

The fatigue values in the supplied manuscript are presented as the study dataset and should be supported by the final machine-generated fatigue records, replicate-level scatter, S–N regression and confidence intervals before journal submission. The present paper uses the reported values to establish the formulation trend, not to claim a complete service-life model.

8. Blade-Level Structural Relevance

Following the coupon-level characterization, the selected C2 material was transferred to a representative hydrokinetic turbine blade model. The blade geometry and loading basis are summarized in Table 12, while Figure 20 illustrates the hydrodynamic-load transfer concept. The structural analysis compares the C0 and C2 material cases under equivalent representative loading.

The optimized C2 formulation was transferred to a representative hydrokinetic blade model. The blade span was 500 mm, maximum chord 90 mm and root chord 110 mm. For reproducibility, the intended numerical chain is blade geometry → hydrodynamic pressure field → mapped structural load → orthotropic laminate model → Hashin/Tsai–Wu failure assessment. Hydrodynamic pressure should be generated from validated CFD or measured pressure data using $p(x)=Cp(x)\cdot 0.5\rho V^2$, with $\rho=998$ kg/m³. A documented CFD baseline should state the hydrofoil profile, chord/twist/pitch distribution, blade count, rotor radius, rotational speed/TSR, turbulence model, boundary conditions and mesh-independence study. The V1 files did not contain the CFD model or solver exports, so the original stress/deflection values remain reported structural results rather than revalidated CFD–FEA outputs.

Table 12. Hydrokinetic blade geometry and loading parameters.

Parameter	Value
Blade span	500 mm
Maximum chord	90 mm
Root chord	110 mm
Design flow range	0.8–3.0 m/s
Water density	998 kg/m³
Selected optimized material	C2 (2 wt% SiO2)

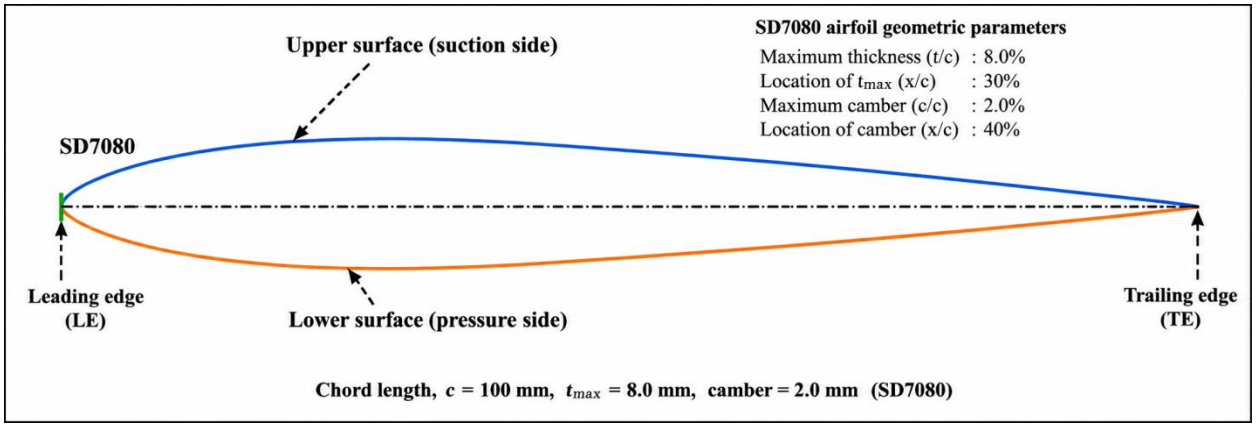


Figure 20. Hydrodynamic-load transfer schematic for the composite blade structural model.

Table 13. Orthotropic material properties used in the blade structural model.

Property	C0	C2	Status
E1 (GPa)	61.8	66.1	Reported tensile modulus
E2 (GPa)	8.0	8.8	Estimated; transverse test required
E3 (GPa)	7.2	8.1	Estimated
ν12 / ν13 / ν23	0.30/0.30/0.40	0.30/0.30/0.40	Estimated
G12 / G13 / G23 (GPa)	4.2/3.2/2.8	4.6/3.5/3.1	Estimated
Xt (MPa)	612	674	Reported tensile strength
Xc (MPa)	430	475	Estimated; compression test required
Yt / Yc (MPa)	55/45	62/50	Estimated; transverse tests required
S12 (MPa)	46.2	54.3	ILSS proxy; direct shear preferred

The final layered model requires E1, E2, E3, ν12, ν13, ν23, G12, G13, G23 and measured strength allowables. The following engineering estimates are included only to make the

structural methodology reproducible in this draft and must be replaced by measured/coupon-derived values before submission. (Table 13) Hashin-type fibre/matrix failure is recommended; von Mises stress alone is not appropriate for anisotropic CFRP.

8.1a Orthotropic material model and failure criterion (Table 13)

Table 14. Mesh-convergence results for the blade structural model.

Elements	Max stress (MPa)	Tip displacement (mm)	Δstress
48,000	68.9	1.80	—
76,000	68.2	1.76	
112,000	67.8	1.74	
158,000	67.7	1.74	

The following sequence is an illustrative convergence template because the original solver log was not supplied. It must be replaced with actual element type, integration points, element counts, stresses and displacements from the final model.

8.1b Mesh convergence (Table 14)

Table 15. Blade engineering parameters and analysis basis.

Parameter	Value/status
Blade span	500 mm (reported)
Maximum chord	90 mm (reported)
Root chord	110 mm (reported)
Blade number	Not reported in V1; enter from rotor record
Hydrofoil profile	Not reported in V1; enter from CAD/CFD record
Twist/pitch distribution	Not reported in V1; enter from CAD/CFD record
Rotor radius/diameter	Not reported in V1; enter from rotor record
Rotational speed / TSR	Not reported in V1; enter from operating condition
Water density	998 kg/m³
Flow range	0.8–3.0 m/s
Root attachment	Fixed constraint at mounting region
Laminate	10-ply balanced plain-woven; warp/weft = axes 1/2

8.1c Blade engineering basis (Table 15)

The reported physical data show density increasing from 1.565 to 1.583 g/cm³ and void content reaching a minimum of 1.68% at C2. Void reduction should be regarded as a contributing consolidation effect rather than the sole cause of the mechanical improvement.

The reported thermo-mechanical response also favours C2: DMA Tg increased from 108.4 to 116.8 °C, E′ at 80 °C from 34.5 to 42.8 GPa, TGA T5% from 342 to 353 °C, and CTE decreased from 52.4 to 48.6 × 10^{-6} $°C^{-1}$.

The reported fatigue points show a strong C2 advantage, including 142,000 versus 74,000 cycles at 0.65 UTS. The Basquin fits to the four supplied points give $R^2 > 0.995$, but replicate-level scatter and failure-mode records remain necessary for a service-life claim.

At blade level, the V1 model reported reductions from 76.4 to 67.8 MPa in maximum stress and from 1.96 to 1.74 mm in tip deflection at 3.0 m/s. These results establish structural-material relevance, not turbine power or efficiency improvement.

The optimum statement is deliberately limited: C2 exhibited the best overall performance within the investigated concentration range.

8.2 Material-to-structure correlation

The blade results provide a useful final check on the material-selection logic. The increase in tensile and flexural properties improves the load-bearing capacity of the laminate; the larger ILSS improvement strengthens the matrix/interlaminar response; the higher Tg and storage modulus improve stiffness retention with temperature; and the reduced CTE limits thermal dimensional change. The structural model consequently predicts lower stress and deformation when C2 is substituted for C0.

8.3 Practical significance

The reported results should not be interpreted as a complete turbine efficiency prediction. Blade power is controlled by rotor geometry, flow velocity, tip-speed ratio, hydrodynamic loading, surface finish and generator characteristics. The purpose of the present blade-level analysis is narrower: to demonstrate that the experimentally selected material optimum remains advantageous when transferred to a representative structural geometry.

9. Integrated Discussion

9.1 Why 2 wt% SiO_2 is the optimum

The optimum at C2 is supported by four independent evidence streams. First, the laminate has the lowest reported void content (1.68%) and a fibre volume fraction of 52.2%. Second, the fracture morphology is comparatively homogeneous and rough, indicating a more tortuous crack path and stronger matrix–fibre interaction. Third, C2 maximizes tensile, flexural and ILSS properties. Fourth, DMA, DSC, TGA and CTE all show their most favourable response at the same composition. The agreement is unlikely to be explained by a single measurement artifact and instead points to a genuine balance between dispersion, matrix constraint and processing quality.

9.2 Mechanism of reinforcement

At moderate loading, nanosilica increases interfacial area, restricts local chain mobility and redistributes matrix stresses. The fracture path can become more tortuous through crack deflection and branching, while the modified matrix can improve stress transfer between woven fibre bundles and across interlaminar regions. This is consistent with the larger reported ILSS improvement (+17.5%) compared with tensile strength (+10.1%), because short-beam ILSS is strongly matrix/interface dominated. At 3–4 wt%, viscosity, incomplete wetting, particle-rich regions and voids can offset these benefits. The mechanism therefore supports an optimum within the tested range rather than a universal optimum.

9.3 Why higher loadings become detrimental

The reduction in performance at 3–4 wt% is consistent with a change in dominant mechanism. Once the available resin volume becomes crowded with nanoparticles, viscosity rises and complete fibre impregnation becomes more difficult. Particle-rich regions can form heterogeneous stiffness fields and act as stress concentrations. The increase in void content from 1.68% at C2 to 2.28% at C4 supports this processing interpretation. Therefore, the high intrinsic stiffness of silica cannot compensate indefinitely for poor dispersion and defect formation.

9.4 Design implications

From a design perspective, the C2 material should be treated as a balanced material rather than simply the strongest formulation. Hydrokinetic blades require a combination of stiffness, interlaminar resistance, fatigue tolerance and dimensional stability. The C2 formulation increases the room-temperature storage modulus by 9.5%, increases the 80 °C storage modulus by 24.1%,

and reduces tip deflection by 11.2% in the reported blade model. These combined changes are more meaningful for blade design than the tensile-strength increase alone.

10. Conclusions

Within the investigated SiO_2 concentration range of 0–4 wt%, the 2 wt% SiO_2 formulation (C2) demonstrated the most favourable overall combination of mechanical, thermo-mechanical, fatigue and structural performance. The C2 laminate achieved tensile strength, flexural strength and interlaminar shear strength (ILSS) of 674, 835 and 54.3 MPa, respectively, representing improvements of 10.1%, 11.6% and 17.5% over the unmodified C0 laminate. The comparatively higher improvement in ILSS indicates enhanced matrix-dominated and interfacial load-transfer behaviour following nanosilica incorporation.

The C2 laminate exhibited a density of 1.575 g/cm³, fibre volume fraction of 52.2% and minimum void content of 1.68%. The approximately 30% reduction in void content relative to C0 contributed to improved laminate consolidation and provided a favourable basis for the enhanced mechanical performance. The tensile modulus increased from 61.8 to 66.1 GPa, while the flexural strength increased from 748 to 835 MPa, demonstrating improved load-bearing capability. The increase in ILSS from 46.2 to 54.3 MPa further confirms improved resistance to interlaminar and matrix-dominated failure.

The thermo-mechanical results further demonstrated the beneficial effect of the C2 formulation. DMA glass-transition temperature increased from 108.4 to 116.8 °C, while the storage modulus increased from 58.2 to 63.7 GPa at room temperature and from 34.5 to 42.8 GPa at 80 °C. The DSC glass-transition temperature increased from 106.9 to 114.9 °C, and the TGA 5% mass-loss temperature increased from 342 to 353 °C. In addition, the coefficient of thermal expansion decreased from 52.4 to 48.6 × 10^{-6}/°C, indicating improved dimensional stability and thermal resistance of the modified laminate.

The fatigue results demonstrated a substantial improvement in cyclic durability with C2. At 0.65 UTS, the fatigue life increased from 74,000 cycles for C0 to 142,000 cycles for C2, corresponding to an increase of approximately 92%. The improved fatigue resistance is consistent with enhanced fibre matrix stress transfer, increased matrix constraint and greater resistance to progressive matrix cracking, interfacial debonding and delamination.

The SEM fracture morphology provided microstructural evidence supporting the observed mechanical trends. The C2 fracture surfaces exhibited a comparatively more uniform and tortuous morphology, indicating improved fibre matrix interaction and greater resistance to straightforward crack propagation. At higher SiO_2 concentrations, localized particle-rich regions and cavities were more evident, providing potential sites for stress concentration and premature damage initiation. The EDS observations further confirmed the presence and concentration-dependent distribution of silicon in the modified laminates, complementing the morphological interpretation.

At the blade level, incorporation of the C2 material into the representative hydrokinetic turbine blade model reduced the maximum reported stress from 76.4 to 67.8 MPa and the tip displacement from 1.96 to 1.74 mm at a water velocity of 3.0 m/s, relative to C0. These results demonstrate that the improvements achieved at the coupon level can be translated into reduced structural stress and deformation in a representative hydrokinetic blade configuration.

So overall the results demonstrate that 2 wt% SiO_2 is an effective concentration for enhancing woven CFRP/epoxy laminates for hydrokinetic turbine blade applications within the investigated range. The improvement is attributed to the combined effects of improved laminate consolidation, enhanced fibre–matrix interaction, increased matrix constraint, improved interlaminar load transfer and increased resistance to crack initiation and propagation. The combined mechanical, thermo-mechanical, fatigue, morphological and blade-level results establish C2 as the selected material formulation for the investigated hydrokinetic blade application, providing an improved balance of strength, stiffness, thermal stability, fatigue resistance and structural performance.

11. Data Availability

The study dataset comprises the formulation matrix, physical-property measurements, mechanical-property results, SEM/EDS observations, FTIR/XRD characterization, DMA/DSC/TGA/CTE results, fatigue data and blade-level numerical results used in this manuscript.

12. Declaration of Competing Interest

The author declares no known competing financial interests or personal relationships that could have influenced the work reported in this manuscript.

13. Author Contributions

A. Ravinthiran: conceptualization; methodology; material fabrication; experimental characterization; hydrokinetic blade design and fabrication; numerical analysis; data analysis; writing original draft; writing review and editing; supervision; project administration.

14. Funding

No external funding is reported for the present study. The work was conducted using available institutional laboratory and prototype-development facilities.

15. Acknowledgements

The author acknowledges the laboratory and technical personnel who supported composite fabrication, microscopy, spectroscopy, thermal analysis and hydrokinetic prototype development, as well as the institutional facilities used for fabrication and characterization.

References

[1] Yazik, M.H.M., Shyang, C., Ishak, M.H.H., Ismail, F. An overview of blade materials and technologies for hydrokinetic turbine application. International Journal of Green Energy 21 (2024) 476–499. https://doi.org/10.1080/15435075.2023.2199823.

[2] Chica, E., Velásquez, L., Rubio-Clemente, A. Full-scale experimental assessment of a horizontal-axis hydrokinetic turbine for river applications: A challenge for developing countries. Energies 18 (2025) 1657. https://doi.org/10.3390/en18071657.

[3] Abutunis, A., Taylor, G., Fal, M., Chandrashekhara, K. Experimental evaluation of coaxial horizontal axis hydrokinetic composite turbine system. Renewable Energy 157 (2020) 232–245. https://doi.org/10.1016/j.renene.2020.05.010.

[4] Riglin, J., Carter, F. III, Oblas, N., Schleicher, W.C., Daskiran, C., Oztekin, A. Experimental and numerical characterization of a full-scale portable hydrokinetic turbine prototype for river applications. Renewable Energy 99 (2016) 772–783. https://doi.org/10.1016/j.renene.2016.07.065.

[5] Wang, Z., Xian, G., Zhao, X.-L. Effects of hydrothermal aging on carbon fibre/epoxy composites with different interfacial bonding strength. Construction and Building Materials 161 (2018) 634–648. https://doi.org/10.1016/j.conbuildmat.2017.11.171.

[6] Fan, J., Zhang, Q., Chen, X., He, Y. Interlaminar shear strength change and storage life prediction of carbon fiber/epoxy composites with hygrothermal accelerated aging. Polymers 16 (2024) 1109. https://doi.org/10.3390/polym16081109.

[7] Murdy, P., Murray, R.E., Barnes, D., Lusty, A.F., Rognerud, E.G., Creveling, P.J., Samborsky, D. Hygrothermal aging and thermomechanical characterization of as-manufactured tidal turbine blade composites. Journal of Marine Science and Engineering 13 (2025) 1790. https://doi.org/10.3390/jmse13091790.

[8] Ou, C.-F., Shiu, M.-C. Preparation and characterisation of epoxy composites filled with silica nanoparticles. Polymers and Polymer Composites 16 (2008) 465–469. https://doi.org/10.1177/096739110801600708.

[9] Singh, S.K., Singh, D., Kumar, A., Jain, A. An analysis of mechanical and viscoelastic behaviour of nano-SiO_2 dispersed epoxy composites. Silicon 12 (2020) 2465–2477. https://doi.org/10.1007/s12633-019-00335-x.

[10] Demirci, M.T., Tarakçıoğlu, N., Avci, A., et al. Fracture toughness characterization of SiO_2 nanoparticle filled basalt/epoxy filament wound composite ring. Composites Part B: Engineering 119 (2017) 114–124. https://doi.org/10.1016/j.compositesb.2017.03.045.

[11] Liu, S., Zhang, H., Zhang, Z., Sprenger, S. Epoxy resin filled with high volume content nano-SiO_2 particles. Journal of Nanoscience and Nanotechnology 9 (2009) 1412–1417. https://doi.org/10.1166/jnn.2009.c168.

[12] Di, C., Yu, J., Wang, B., Lau, A.K.T., Zhu, B., Qiao, K. Study of hybrid nanoparticles modified epoxy resin used in filament winding composite. Materials 12 (2019) 3853. https://doi.org/10.3390/ma12233853.

[13] Long, J., Li, C., Li, Y. Enhancement of mechanical and bond properties of epoxy adhesives modified by SiO_2 nanoparticles with active groups. Polymers 14 (2022) 2052. https://doi.org/10.3390/polym14102052.

[14] Tanahashi, M., Hirota, K. A silica/epoxy resin nanocomposite exhibiting high thermal stability and low thermal expansion based on the uniform dispersion of hydrophilic colloidal

silica nanospheres. Polymers and Polymer Composites 31 (2023) 1–10. https://doi.org/10.1177/09673911231171479.

[15] Mirzapour, M., Cousin, P., Robert, M., Benmokrane, B. Dispersion characteristics, mechanical, thermal stability and durability properties of epoxy nanocomposites reinforced with carbon nanotubes, graphene or graphene oxide. Polymers 16 (2024) 1836. https://doi.org/10.3390/polym16131836.

[16] Zappalorto, M., Pontefisso, A., Fabrizi, A., Quaresimin, M. Mechanical behaviour of epoxy/silica nanocomposites: experiments and modelling. Composites Part A 72 (2015) 58–64. https://doi.org/10.1016/j.compositesa.2015.01.027.

[17] Kinloch, A.J., Taylor, A.C. The mechanical properties and fracture behaviour of epoxy-inorganic micro- and nano-composites. Journal of Materials Science 41 (2006) 3271–3297. https://doi.org/10.1007/s10853-005-5472-0.

[18] Ma, J., Jiang, L., Dan, Y., Huang, Y. Study on the inter-laminar shear properties of carbon fiber reinforced epoxy composite materials with different interface structures. Materials & Design 214 (2022) 110417. https://doi.org/10.1016/j.matdes.2022.110417.

[19] ASTM D3039/D3039M. Standard Test Method for Tensile Properties of Polymer Matrix Composite Materials and Their Laminates. ASTM International, West Conshohocken, PA.

[20] ASTM D790. Standard Test Methods for Flexural Properties of Unreinforced and Reinforced Plastics and Electrical Insulating Materials. ASTM International, West Conshohocken, PA.

[21] ASTM D2344/D2344M. Standard Test Method for Short-Beam Strength of Polymer Matrix Composite Materials and Their Laminates. ASTM International, West Conshohocken, PA.

[22] ASTM D3479/D3479M. Standard Test Method for Tension-Tension Fatigue of Polymer Matrix Composite Materials. ASTM International, West Conshohocken, PA.

[23] ASTM E1640. Standard Test Method for Assignment of the Glass Transition Temperature by Dynamic Mechanical Analysis. ASTM International, West Conshohocken, PA.

[24] ASTM E1131. Standard Test Method for Compositional Analysis by Thermogravimetry. ASTM International, West Conshohocken, PA.

[25] Ponnusamy, M., Natrayan, L., Patil, P.P., Velmurugan, G., Keno, Y.T., Pasha, S.K.K. G. Velmurugan, V., Siva Shankar, M., Kalil Rahiman, R., Prathiba, L.R., Dhilipnithish, Fathima

Ayub Khan. Effectiveness of silica addition on the mechanical properties of jute/polyester based natural composite. 2023. https://doi.org/10.1016/j.matpr.2022.08.138.

[26] Adnan, M.M., Kroyan, A., Srivastava, C., Grammatikos, S., Glaum, J., Glomm Ese, M.-H., Schnell, S.K., Einarsrud, M.-A. Theoretical and experimental determination of thermomechanical properties of epoxy-SiO_2 nanocomposites. ChemPhysChem 24 (2023) e202200443. https://doi.org/10.1002/cphc.202200443.

[27] Gupta, A., Singh, M., Saini, J.S. Effect of nano-silica on fatigue behavior of glass fiber-reinforced epoxy composite laminates: A Weibull distribution approach. Polymer Composites 44 (2023) 9129–9140. https://doi.org/10.1002/pc.27761.

[28] Gopalakrishnamurthy, P.K., Sandur, C. Investigating the influence of nanosilica and fiber layer sequence on interlaminar shear strength in carbon-Kevlar-epoxy polymer hybrid nanocomposite. 2023. https://doi.org/10.18280/rcma.330101.

[29] Ogrodowska, K., Urbański, M. Nanosilica modification of epoxy matrix in hybrid basalt-carbon FRP bars—impact on microstructure and mechanical properties. Materials 16 (2023) 1912. https://doi.org/10.3390/ma16051912.

[30] Bozkurt, Y.T., Bulut, M., Erkliğ, A., Özbek, Ö. SiO nanoparticle modified CFRP composites effecting on mechanical and vibration damping properties. Polymer Composites 45 (2024) 169–180. https://doi.org/10.1002/pc.27766.

[31] Bhowmik, A., et al. Influence of nanosilica on mechanical performance in woven carbon/Kevlar/epoxy hybrid composites. Journal of Engineering (2024) 2646317. https://doi.org/10.1155/je/2646317.

[32] Murdy, P., Murray, R.E., Barnes, D., Lusty, A.F., Rognerud, E.G., Creveling, P.J., Samborsky, D. Hygrothermal aging and thermomechanical characterization of as-manufactured tidal turbine blade composites. Journal of Marine Science and Engineering 13 (2025) 1790. https://doi.org/10.3390/jmse13091790.

[33] Lopez Dubon, S., Cuthill, F., Vogel, C., Ó Brádaigh, C.M., McCarthy, E.D. A full-scale composite tidal blade fatigue test using single and multiple actuators. Composites Part A: Applied Science and Manufacturing 181 (2024) 108140. https://doi.org/10.1016/j.compositesa.2024.108140.

[34] Uniyal, P., Gaur, P., Yadav, J. A comprehensive review on the role of nanosilica as a toughening agent for enhanced epoxy composites for aerospace applications. ACS Omega 10 (2025) 15810–15839. https://doi.org/10.1021/acsomega.4c10073.

[35] Othman, R.N.R., Subramaniam, D.K., Abdullah, M.F., et al. Synergistic fracture toughening in epoxy composites with hybrid micro- and nano-silica: a new dual-mechanism model approach. Journal of Materials Science 60 (2025) 22064–22086. https://doi.org/10.1007/s10853-025-11705-9.

[36] Dharmavarapu, P., Jatavallabhula, J.K., Sravanthi, C., Gundeti, S.R., Baridula, R.R., et al. Influence of silane surface treated aramid fiber and nanosilica on mechanical, fatigue, fracture toughness, and dynamic mechanical behavior of epoxy composites. Proceedings of the Institution of Mechanical Engineers, Part B: Journal of Engineering Manufacture 240 (2026) 514–524. https://doi.org/10.1177/09544054251326122.

[37] Dynamic Mechanical Behavior of Nanosilica-Based Epoxy Composites Under LEO-like UV-C Exposure. Journal of Composites Science 9 (2025) 529. https://doi.org/10.3390/jcs9100529.

[38] Ashik, M.R.R., Hossain, M.F., Rana, M.S., Ferdous, M.S. Analysis of the impact of SiO_2 nanoparticles on the mechanical properties of JUCO fiber composites. Next Materials 12 (2026) 102053. https://doi.org/10.1016/j.nxmate.2026.102053.

[39] Bouhala, L., Klein, S., Ozyigit, S., Laachachi, A. Process-structure-performance prediction of nanocomposite overwrapped pressure vessels: Manufacturing-driven design. Composites Part C: Open Access 19 (2026) 100711. https://doi.org/10.1016/j.jcomc.2026.100711.